

Mass-scaling as a method to constrain outflows and particle acceleration from low-luminosity accreting black holes

R. M. T. Connors,^{1*} S. Markoff,¹ M. A. Nowak,² J. Neilsen,² C. Ceccobello,¹
P. Crumley,¹ C. S. Froning,³ E. Gallo,⁴ J. E. Nip^{1†}

¹*Anton Pannekoek Institute, University of Amsterdam, Science Park 904, 1098 XH Amsterdam, The Netherlands*

²*Massachusetts Institute of Technology, Kavli Institute for Astrophysics, Cambridge, MA 02139, USA*

³*Department of Astronomy, C1400, University of Texas at Austin, Austin, TX 78712, USA*

⁴*Department of Astronomy, University of Michigan, Ann Arbor, MI 48109-1042, USA*

ABSTRACT

The ‘fundamental plane of black hole accretion’ (FP), a relation between the radio luminosities (L_R), X-ray luminosities (L_X), and masses (M_{BH}) of hard/quiescent state black hole binaries and low-luminosity active galactic nuclei, suggests some aspects of black hole accretion may be scale invariant. However, key questions still exist concerning the relationship between the inflow/outflow behaviour in the ‘classic’ hard state and quiescence, which may impact this scaling. We show that the broadband spectra of A0620-00 and Sgr A* (the least luminous stellar mass/supermassive black holes on the FP) can be modelled simultaneously with a physically-motivated outflow-dominated model where the jet power and all distances are scaled by the black hole mass. We find we can explain the data of both A0620-00 and Sgr A* (in its non-thermal flaring state) in the context of two outflow-model scenarios: (1) a synchrotron-self-Compton dominated state in which the jet plasma reaches highly sub-equipartition conditions (for the magnetic field with respect to that of the radiating particles), and (2) a synchrotron dominated state in the fast-cooling regime in which particle acceleration occurs within the inner few gravitational radii of the black hole and plasma is close to equipartition. We show that it may be possible to further discriminate between models (1) and (2) through future monitoring of its submm/IR/X-ray emission, in particular via time lags between the variable emission in these bands.

Key words: accretion, accretion discs – black hole physics – galaxies: jets – radiation mechanisms: non-thermal – X-rays: binaries – Galaxy: centre.

1 INTRODUCTION

Accreting black holes span an enormous range of masses, from black holes in stellar X-ray binaries (BHBs) of a few M_\odot to active galactic nuclei (AGN) harbouring supermassive black holes (SMBH) ranging from $\sim 10^6$ – $10^{10} M_\odot$. The accretion physics of BHBs has been extensively studied, and their accretion evolution is well characterised by a disc instability model (see [Lasota 2001](#) for a review). Observationally, BHBs (high mass and low mass alike) are classified via particular ‘states’ based on their spectral and timing properties, of which there are many (e.g. [Nowak 1995](#); [Gierliński & Done 2003](#); [Remillard & McClintock](#)

[2006](#); [Belloni 2010](#)), but the two longest-lived and thus ‘canonical’ states are the so-called ‘hard’ and ‘soft’. A basic underlying definition can be given to the hard and soft states of BHBs, wherein hard refers to an X-ray spectrum dominated by higher energies (> 10 keV) and a non-thermal power-law spectrum, and soft is dominated by lower X-ray energies (2–10 keV) and a thermal blackbody spectrum. An idea currently under exploration concerns observational comparisons between AGN and BHBs that point to an identification of some AGN classifications with BHB states (e.g. [Körding, Jester & Fender 2006](#)).

Whilst the classic thermal-blackbody thin accretion disc component provides a good model representation of the soft state ([Shakura & Sunyaev 1973](#)), there is not yet an agreed upon paradigm for the hard state. This latter situation is well demonstrated in the case of Cyg X-1

* E-mail: r.m.t.connors@uva.nl

† Current e-mail: jonathannip@gmail.com

(a well-studied BHB with a high mass companion star), wherein multiple models with different inflow/outflow geometries (thermal/non-thermal coronae, jets) are all capable of explaining the observed hard-state X-ray spectrum (Nowak et al. 2011): spectral modelling of BHBs in the hard state is degenerate. Furthering our understanding of the accretion, ejection and radiative processes of BHBs thus calls for novel methods to strip out this spectral fitting degeneracy and determine how gravitational energy is re-distributed in the hard state.

Observations of BHBs at both radio and X-ray wavelengths during the hard state, which we define now as sources having an Eddington scaled X-ray luminosity (L_X) in the range $L_X/L_{\text{Edd}} \equiv l_X \sim 10^{-6}$ – 10^{-2} ¹, reveal a correlation between the respective luminosities, $L_X \propto L_R^{0.6-0.7}$ (Corbel et al. 2000, 2003; Gallo, Fender & Pooley 2003; Corbel, Körding & Kaaret 2008; Corbel et al. 2013, see also Miller-Jones et al. 2011 and Gallo et al. 2014). This scaling relation indicates a coupling between the radio/X-ray emission mechanisms during the hard state, pointing to a connection between the accretion flow and the jet—since radio emission in BHBs is identified with a steady compact jet, as directly imaged in BHBs GX 339-4, Cyg X-1, and GRS 1915+105 (Fender 2001; Stirling et al. 2001; Miller-Jones et al. 2005). This scaling relation also presents the possibility of breaking model degeneracies (discerning the dominant spectral components in hard state BHBs).

This concept of scaling has broader implications when we compare these hard state BHBs with AGN showing similar compact jets, since a common scaling would imply the discovered correlation (and thus inflow/outflow coupling in these particular states) is independent of black hole mass. It has been shown that when one includes low-luminosity AGN with jet cores (low-luminosity AGN (LLAGN): including LINERS, FR1, and BL Lacs), the correlation extends to the so-called Fundamental Plane of Black Hole Accretion (FP), relating the X-ray luminosities, L_X , radio luminosities, L_R , and masses, M_{BH} of the selected LLAGN and hard-state BHBs (Merloni, Heinz & Di Matteo 2003; Falcke, Körding, & Markoff 2004; Körding, Falcke & Corbel 2006; Plotkin et al. 2012). Efforts to derive these scaling laws begin by expressing all luminosities in terms of their dependence on mass and mass-accretion rate (expressed in mass-scaling Eddington units $\dot{m} = \dot{M}/\dot{M}_{\text{Edd}}$, where $\dot{M}_{\text{Edd}} = L_{\text{Edd}}/(0.1c^2)$). For example, it can be shown through full calculation of the scaling relations that in order to satisfy the observed correlation, weakly accreting black holes must be radiating inefficiently ($L \propto \dot{m}^q$, where $q \approx 2$) (Markoff et al. 2003; Heinz & Sunyaev 2003; Plotkin et al. 2012); which includes synchrotron, inverse Compton and bremsstrahlung processes.

There are prevalent difficulties with attempts to distinguish between these allowed radiative processes, and thus accretion models, capable of reproducing this $L \propto \dot{m}^2$ dependence, due primarily to the degeneracy

in spectral modelling. For instance various radiatively inefficient accretion flow (RIAF) models (Narayan & Yi 1994; Yuan, Quataert & Narayan 2003) and outflow models (Yuan, Markoff & Falcke 2002; Yuan, Cui & Narayan 2005) have the inefficient ($q \approx 2$) scaling predicted by the FP. In addition to broadband spectral modelling, degeneracies can be disentangled by introducing further observational data, such as X-ray variability studies (van der Klis 1995; Remillard & McClintock 2006), broadband variability studies (Casella et al. 2010; Gandhi et al. 2010; Kalamkar et al. 2016), variability comparisons of AGN and BHBs (Uttley & McHardy 2005; McHardy et al. 2006), and polarisation measurements (Shahbaz et al. 2008; Russell & Fender 2008). Sgr A*, the SMBH at the Galactic centre, is a prime example of how combining these individual diagnostics leads to a better physical interpretation of the emission mechanisms (Bower et al. 2003; Genzel et al. 2003; Ghez et al. 2004; Eckart et al. 2006; Marrone et al. 2006; Witzel et al. 2012; Neilsen et al. 2015; Li et al. 2015; Dibi et al. 2016). However, even with all such techniques, degeneracies still exist in the physical interpretation of the hard X-ray emission mechanisms of hard state BHBs and LLAGN. Markoff et al. (2015) attempt a new approach in breaking the degeneracy between the SSC and synchrotron-dominated scenarios, testing the extent to which the scale invariance implied by the FP holds. They jointly model the broadband spectral energy distributions (SEDs) of two black holes on opposite ends of the mass scale (the LLAGN M81*, and the BHB V404 Cyg in a low-luminosity hard state), accreting at similar Eddington rates ($l_X \sim 10^{-6}$). The same model with half of the fitted parameters at the same value (in mass-scaled units) provides a good fit to both sources, and a model in which synchrotron emission dominates the high-energy spectra provides the most reasonable fit.

Now that a proof-of-concept has shown the method of joint spectral modelling provides physical insight into black holes across the mass scale, we want to extend the study to quiescence ($l_X < 10^{-6}$). Is quiescence a direct continuation of the hard state, or does the physics change below some accretion rate, as indicated by the increase in the X-ray power-law spectral index (Kong et al. 2002; Tomsick et al. 2003; Tomsick, Kalemci & Kaaret 2004; Corbel, Tomsick & Kaaret 2006; Corbel, Körding & Kaaret 2008; Plotkin, Gallo & Jonker 2013)? Plotkin et al. (2015) model the broadband spectrum of BHB XTE J1118+480 in its quiescent state and compare to previous modelling of its hard state emission (Maitra et al. 2009), showing that the transition from the hard to quiescent state of XTE J1118+480 may be characterised by a decrease in particle acceleration efficiency (see e.g. Markoff 2010)—it is also interesting to note that the radio/X-ray correlation slope of XTE J1118+480 is consistent with those of other sources on the trend over 5 dex in l_X . Here we adopt the method presented in Markoff et al. (2015), fitting an outflow-dominated model (the details of which can be found in Markoff, Nowak & Wilms 2005 and Maitra et al. 2009, from here on MNW05 and M09 respectively) to two black holes deep in quiescence yet on opposite ends of the mass scale; quiescent ($l_X \sim 10^{-8.5}$) BHB A0620-00 and SMBH Sgr A* ($l_X \sim 10^{-9}$ during bright, non-thermal flares).

¹ $L_{\text{Edd}} = 4\pi GMm_p c/\sigma_T = 1.25 \times 10^{38} (M/M_\odot) \text{ erg/s}$, where G is the gravitational constant, m_p is the proton mass, c is the speed of light, σ_T is the Thomson cross-section, M is the black hole mass, and M_\odot is the mass of the Sun.

In Sections 2 and 3 we give an overview of the theoretical and observational history (and therefore the source properties determined to date) of Sgr A* and A0620-00 respectively and a brief description of the data used in our modelling. In Section 4 we describe the model (including the updates made to the model in Sections 4.1 and 4.2) we apply to both sources. In Section 5 we describe the methodology behind fitting the broadband spectra. In sections 6 and 7 we present results of individual fits to both sources, as well as the new joint fits. In section 8 we discuss which of our model scenarios are most plausible when applied to both sources, and posit possible future observations and work.

2 Sgr A*

Our own galaxy harbours an extremely weakly accreting SMBH, Sgr A*, that during intermittent non-thermal flaring seems to fit the criteria of a source in the universally regulated state associated with the FP (see Melia & Falcke 2001, Markoff 2005, Genzel, Eisenhauer & Gillessen 2010, Markoff 2010 and Yuan & Narayan 2014 for full reviews on the features of Sgr A* and the Galactic centre). Sgr A* has a mass of $4.1 \times 10^6 M_\odot$ (Genzel et al. 2003; Ghez et al. 2008; Gillessen et al. 2009) and lies at a distance of 8 kpc (Reid 1993; Ghez et al. 2008; Reid et al. 2009). The unabsorbed X-ray (2–10 keV) luminosity of Sgr A* during quiescence is a few times 10^{33} erg s⁻¹ (Baganoff et al. 2003) or $l_X \sim 10^{-11}$, making it the most weakly accreting black hole observed to date. Wang et al. (2013) present the results of 3 Msec of *Chandra X-ray Observatory* imaging of the Galactic centre as part of an X-ray Visionary Project (see <http://www.sgr-star.com>), resolving the accreting gas around Sgr A* during quiescence. The results confirm that the steady quiescent spectrum of Sgr A* can be fit with a thermal bremsstrahlung model from a hot plasma near the Bondi radius, consistent with earlier predictions by e.g. Narayan, Yi & Mahedevan (1995); Quataert (2002).

Frequent X-ray monitoring of Sgr A* also resulted in the discovery of flares (Baganoff et al. 2001) lasting as long as 10 ks with a peak luminosity ~ 50 x brighter than the quiescent emission, with the flare emission best fit by a power law with a significantly harder spectrum than that detected in quiescence ($dI_\nu/d\nu = \nu^{-\alpha}$, $\alpha \sim 0.3$, with $\alpha \sim 1.2$ in quiescence). Subsequent observations of the flare emission have found peak luminosities reaching 130x (Nowak et al. 2012) and 400x (Haggard et al., in prep.) higher than the quiescent level, originating from much smaller radii than the quiescent emission. Attempts to model the variable (flare) emission of Sgr A* now include jet models capable of producing a synchrotron + inverse Compton (in particular SSC) (Falcke & Markoff 2000; Markoff et al. 2001), and hybrid models including RIAF components, both thermal (Yuan, Markoff & Falcke 2002) and with a non-thermal population of particles (Yuan, Quataert & Narayan 2003). The 3 Msec of additional observing time with *Chandra* allowed the first detailed observations of the flaring emission, doubling the population of known flares within a year (Neilsen et al. 2013). These flares range in duration from a few 100 seconds to 8 ks, and in luminosity from $\sim 10^{34}$ erg s⁻¹ to 2×10^{35} erg s⁻¹, bringing Sgr A* to fluxes consistent

with the FP relation (in quiescence Sgr A* lies ~ 2 orders of magnitude in L_X below the FP relation). The timescales of the flares indicate an emission region of 5–400 r_g , though large excursions from quiescence likely originate from within $\approx 5 r_g$ (Barri re et al. 2014).

We are interested in modelling Sgr A* during bright X-ray flares (when Sgr A* approaches the FP relation), and thus we select the 3 brightest X-ray flares, with peak count rates 0.15–0.25 cts/s, whereby this grouping of flares contains sufficient cumulative counts for us to perform χ^2 statistics—see Figure 1. The details of the *Chandra* observations and data reduction can be found in Neilsen et al. (2013), and in section 5.1 we detail how the spectra are binned/grouped and subsequently modelled.

X-ray flares observed from Sgr A* are coincident with an IR counterpart, but the opposite is not always true (Eckart et al. 2006; Hornstein et al. 2007). This characteristic hints at the nature of the physical connection between the IR/X-ray emission, however lack of coverage combined with uncertainties regarding the IR flux distribution make simultaneous modelling a difficult task (Dodds-Eden et al. 2011; Trap et al. 2011; Witzel et al. 2012). We thus select the median IR H and ks-band fluxes found by Bremer et al. (2011), 3.61 ± 1.62 and 6.03 ± 1.85 mJy respectively, and the mid-IR 3σ upper limit of 58 mJy found by Haubois et al. (2012). Using the median NIR fluxes allows us to somewhat represent the flux uncertainties during the brightest X-ray flares, whilst the mid-IR upper limit allows us to put prior constraints on our model parameters (since the thermal synchrotron spectrum cannot exceed this upper limit).

We require a quasi-simultaneous broadband spectrum to perform time-independent modelling. Sgr A* only becomes significantly variable (up to $\sim 40\%$) at submm wavelengths, when the emitting region is optically thin (Lu et al. 2011; Bower et al. 2015), though there has been a rise in flux of $\sim 20\%$ in the 5–20 GHz range over the past decade (An et al. 2005; Bower et al. 2015), as shown in Figure 2. We compile an average radio-to-submm spectrum that encompasses this short and long term variability, with appropriate coverage across the 330 MHz - 850 GHz range. The resulting data table can be found in Table A2 in the Appendix.

3 A0620-00

First discovered at X-ray wavelengths when it went into outburst in 1975 (Elvis et al. 1975), A0620-00 (hereafter A0620) settled into quiescence 15 months later. It has been in a persistent quiescent state since then, and we now know that the system consists of a K-type donor star transferring mass to a black hole via an accretion disc (McClintock & Remillard 1986). The mass, distance, and orbital inclination (i) are found by Cantrell et al. (2010) to be $6.6 \pm 0.25 M_\odot$, 1.06 ± 0.12 kpc and $51.0^\circ \pm 0.9$ respectively. Garcia et al. (2001) and Kong et al. (2002) find a quiescent X-ray luminosity for A0620 of 3×10^{30} erg s⁻¹, which corresponds to $\sim 10^{-8.5} L_{\text{Edd}}$, whilst Gallo et al. (2006) find $L_X = 7.1^{+3.4}_{-4.1} \times 10^{30}$ ergs⁻¹, which also puts A0620 in the Eddington range $l_X \sim 10^{-9}$ – $10^{-8.5}$. Given the implication of the FP that black holes accreting at similar Eddington rates should regulate their output in the same way, A0620 is a suitable candidate for a comparison study with Sgr A* in

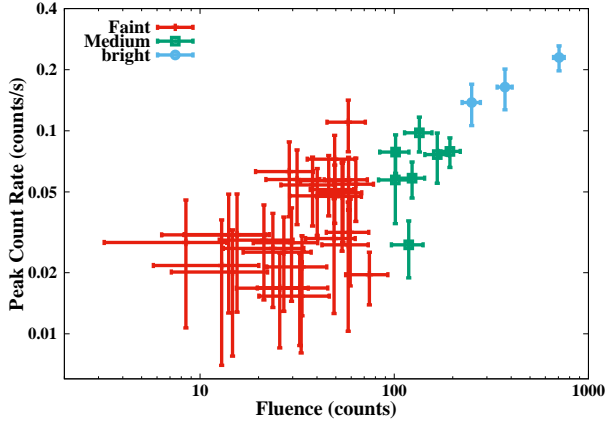


Figure 1. The splitting of X-ray flares into 3 categories of peak count rate. The plot shows how the 39 X-ray flares (Neilsen et al. 2013) are divided into 3 sections, based on CF levels ≤ 1200 (red lines), $1200 \leq CF \leq 2200$ (green squares), and $CF > 2200$ (blue circles).

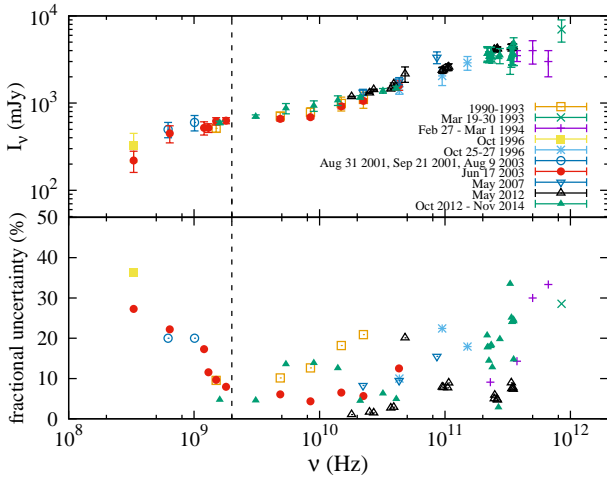


Figure 2. The radio to submm spectrum of Sgr A* as observed over the past 20 years. The key shows the observing windows of the following works in order from top to bottom; Zhao, Bower & Goss (2001); Serabyn et al. (1997); Zylka et al. (1995); Nord et al. (2004); Falcke et al. (1998); Roy & Rao (2004); An et al. (2005); Lu et al. (2011); Brinkerink et al. (2015); Bower et al. (2015). The top panel shows the mean flux density as a function of frequency ranging from 330 MHz to 850 GHz. The bottom panel shows the fractional uncertainty (uncertainty/flux) of each flux measurement. The dotted line shows the boundary below which measurement uncertainty due to the scattering screen of electrons along the line of sight starts to dominate the intrinsic variability of Sgr A*.

its non-thermal ‘flaring’ state.

A0620 has an 8.5 GHz radio flux density of $51 \pm 7 \mu\text{Jy}$ (Gallo et al. 2006), interpreted as self-absorbed synchrotron emission from a jet/outflow. Comparison of the radio/X-ray flux confirms A0620 as the lowest-luminosity source on the FP. Mid-IR detections suggest the self-absorbed synchrotron emission extends up to the mid-IR given the flat spectral index between radio-mid-IR, though a circumbinary disc component cannot be ruled out (Muno & Mauerhan 2006; Gallo et al. 2007).

Froning et al. (2011) present a broadband spectral energy distribution (SED) including X-ray, UV, optical, NIR, and radio observations of A0620, adding to the already existing broadband coverage (Narayan, McClintock & Yi 1996; McClintock & Remillard 2000; Gallo et al. 2006, 2007). Through modelling of the broadband spectrum, Froning et al. (2011) show that 90 % of the disc mass is lost between the outer and inner accretion flow, indicative of either an outflow prior to capture by the black hole (an ADIOS-like solution, e.g. Blandford & Begelman 1999, 2004), or mass loss to the black hole (an ADAF-like solution, e.g. Narayan & Yi 1994). Wang et al. (2013) find a similar accretion disc density profile explains the low accretion rates onto Sgr A*, providing a further analogy between black holes of varying mass accreting at very sub-Eddington rates. Since A0620 extends the radio/X-ray correlation down to the most quiescent luminosities, and we know that brighter hard-state sources show a radio jet, it seems reasonable to assume the presence of a jet at the lowest luminosities.

We model the full radio-to-X-ray quasi-simultaneous spectrum of A0620. This includes the simultaneous radio/IR/optical/X-ray observations taken in August 2005 presented by Gallo et al. (2006), the IR observations taken 5 months prior in March 2005 by (Gallo et al. 2007), and full IR/optical/UV observations taken by Froning et al. (2011) in March 2010. We refer the reader to the relevant observational papers for a full description of the data reduction and analysis. Combining these datasets gives us good coverage from radio to X-ray frequencies whilst accounting for the optical/UV variability of A0620 during its ‘active’ state (Cantrell et al. 2008). Although this results in added χ^2 residuals in our fits, it is more informative to include this variability and have a representative time-averaged spectrum. We also note that the constraints that come from fitting across 8 orders of magnitude in spectral energy outweigh the residuals accrued by modelling data over these two epochs (see e.g. Markoff et al. 2008). We deredden the IR-FUV fluxes with $E(B - V) = 0.39$ in agreement with Gallo et al. (2007). The full radio-FUV dereddened flux values are shown in table A1 in the Appendix. The X-ray spectrum is identical to that modelled in Gallo et al. (2007).

4 THE MODEL

We explore statistical fits of the `agnjet` model (MNW05, M09) to multiwavelength spectra of both Sgr A* and A0620 separately, and then perform joint fitting of both sources, tying parameters that represent the scale invariance (this is discussed in detail in Section 7).

MNW05 and M09 (and references therein) give a full description of `agnjet` including its assumptions and parameters, and subsequent work explores model fits to both BHs and LLAGN (Plotkin et al. 2015; Markoff et al. 2015; Prieto et al. 2016). Here we give a basic outline and a description of the `agnjet` parameters. In `agnjet`, a relativistic plasma of adiabatic index $\Gamma = 4/3$ is injected in a nozzle at the base of the jet (or rather both axially symmetric jets) following assumptions for the hydrodynamics as laid out in Falcke & Biermann 1995; Falcke 1996. At the jet base, the internal energy density, $U_J = U_B + U_e + U_{tu}$ (where U_B is the magnetic energy density, U_e is the relativistic elec-

Table 1. A list of the main input parameters of the `agnjet` model

Parameter	Description
N_j	the normalised jet power, in units of L_{Edd} .
r_0 and h_0 (r_g)	the radius and height (length) of the jet nozzle.
T_e (K)	the electron temperature of the input distribution.
k	the ratio of magnetic to electron energy density, U_B/U_e , otherwise known as the partition factor.
p	the power-law index of the accelerated electron distribution.
z_{acc} (r_g)	the distance from the black hole along the jet axis where particle acceleration begins.
n_{nth}	the fraction of particles accelerated at a distance z_{acc} from the black hole along the axis of the jet.
f_{sc}	$\beta_{\text{sh}}^2/(\lambda/R_{\text{gyro}})$ where β_{sh} is the shock speed relative to the plasma, λ is the scattering mean free path in the plasma at the shock region, and R_{gyro} is the gyroradius of the particles in the magnetic field. In reality we do not require a shock so this parameterisation can generally be seen as a measure of the acceleration efficiency.
ϵ_{nth}	the fraction of energy density in non-thermal electrons injected at the jet base.
Δ_{fac}	the multiplication factor giving the maximum energy of the injected non-thermal electrons, $\gamma_{\text{max,nth}} = \Delta_{\text{fac}}\gamma_{\text{min,nth}}$.

Notes. Parameters ϵ_{nth} and Δ_{fac} only apply in model cases (c) and (d), when a mixed distribution of thermal and non-thermal particles is injected at the base of the jet.

tron energy density, and U_{tu} is the turbulent plasma energy density), is assumed to be equal to the rest-mass energy density. [Zdziarski \(2016\)](#) points out that in fact the internal energy density could be arbitrarily large. However, the small Lorentz factors found in BHB jets ($\gamma_j \sim$ a few), as well as implied by the variability in Sgr A* ([Falcke, Markoff, & Bower 2009](#); [Brinkerink et al. 2015](#)), require that the jet's internal energy density not exceed the rest-mass energy density by a factor of more than a few at the base of the jet. We therefore suggest that such a scenario applies for all low-luminosity sources (lying on the FP) such as Sgr A* and A0620. Limiting the internal energy density of the jet in this way means we are not describing what would be classed as a Poynting-flux dominated jet ([Blandford & Znajek 1977](#)) in any of our modelling; we cannot have $U_B > nm_p c^2$, since the dynamics are not correctly calculated in such a scenario. In that sense our jet is consistent with being matter-dominated ([Blandford & Payne 1982](#)).² The plasma is assumed to expand freely with an initial sound speed $\beta_{s,0} = \sqrt{\Gamma(\Gamma - 1)/(\Gamma + 1)} \sim 0.43$ in the lateral direction, and longitudinal pressure gradients accelerate the jet to supersonic speeds along its axis.

The main parameters of interest are displayed in [Table 1](#). The most important fitted parameter here is N_j , the

² We are currently exploring extending the `agnjet` model to cases in which the internal energy density of the plasma is not equal to the rest-mass energy density at the jet nozzle. We will address this topic in detail in a forthcoming research note ([Crumley et al., in prep.](#)), since it resides outside the scope of this paper.

normalised jet power, since it acts as the model normalisation, and the entire spectrum is very sensitive to its value. N_j is thus the total power fed into the base of the jet. Since the jet base represents a steady state, the inflow rate given by the power and the initial sound speed ($\beta_{s,0}$) and nozzle radius (r_0) sets the energy density. The partition factor k parameterises the division of the jet energy density between the magnetic field and electrons (U_B/U_e)³, where $k \sim 1$ is referred to as equipartition. Since there is no radial structuring in `agnjet`, once r_0 is known the radial jet profile $r(z)$ is calculated, defining the jet opening angle by evaluating the velocity profile along the jet, a solution to the relativistic Euler equation for a roughly isothermal jet ([Falcke 1996](#)). The radius of the jet base r_0 is a very influential parameter, since the initial energy density comprising the magnetic field and particles depends inversely on the square of the radius ($U \propto r_0^{-2}$). Thus decreasing the jet-base radius increases the radiative output significantly, and it also affects the synchrotron/SSC radiative outputs differently. The height h_0 has an effect, though somewhat less than the radius. Increasing the height of the nozzle will cause an increase in the thermal synchrotron flux, as well as provide more particles to inverse Compton upscatter the synchrotron photons. We explore this parameter during fitting by both fixing it and allowing it to vary freely to explore SSC-dominated fits.

The particles entering the base of the jet are assumed to be advected from the accretion flow with a thermal distribution at temperature T_e (we note that this temperature may be different to the equilibrium temperature of the accretion flow, due to any heating processes at work), and are subsequently accelerated into a power law energy distribution at a distance z_{acc} from the black hole along the axis of the jet (also a free parameter). An additional parameter n_{nth} is included to specify the fraction of these particles accelerated into the power law (this is a separate parameterisation from ϵ_{nth} , the fraction of energy density in non-thermal electrons injected at the jet base, discussed in [Section 4.2](#)), which we initially fix at 0.6, reflective of typical values used in previous applications of `agnjet` (MNW05, M09). We represent the acceleration rate efficiency with the parameter f_{sc} , which incorporates uncertainty in the acceleration mechanism, and whose derivation is presented in [Jokipii \(1987\)](#). We stress that we are not asserting that the mechanism must be diffusive shock acceleration, but rather these are convenient parameterisations of acceleration in general.

Additional parameters include the inner temperature and radius of the accretion flow, T_{in} and r_{in} , used to describe the thermal accretion disc blackbody emission, and these photons are included in the photon field which undergoes inverse Compton scattering at low optical depth (a maximum of one scattering per photon) with the jet electrons. These are not included in [Table 1](#) because for both Sgr A* and A0620 there is no discernible thin disc component to model; in the case of Sgr A* we adopt a bremsstrahlung model to fit the quiescent thermal spectrum ([Wang et al. 2013](#)), assumed to be produced by a RIAF as discussed in [Section 2](#). Fixed parameters include the mass of the black hole, M_{BH} , the inclination of the jet axis to the line of sight, θ_i , and the

³ This is essentially the inverse of the plasma beta parameter ($k = 1/\beta$).

distance to the source, D .

The model `agnjet` produces 3 main components of emission—thermal synchrotron (at $z < z_{acc}$), non-thermal synchrotron (produced at $z > z_{acc}$), and SSC (with a contribution from inverse Compton scattering of disc photons, a minimal component in fits to Sgr A* and A0620)—and as previously discussed in Section 1, there is significant degeneracy between these components when fitting the spectra of hard-state BHBs and LLAGN, particularly the X-ray spectra. The jet becomes self-absorbed once it becomes optically thick at a given frequency, and hence exhibits a spectral break (also often referred to as the spectral turnover or self-absorption frequency) at ν_{SSA} below which we see the flat/inverted radio spectrum.

4.1 Synchrotron cooling

The accelerated distribution of electrons had in previous versions of `agnjet` been assumed to be maintained by dissipative processes along the post-acceleration regions of the jet, with no prescription for the cooling of electrons due to synchrotron radiation (Falcke & Markoff 2000, MNW05, M09, Plotkin et al. 2015, Markoff et al. 2015). We have updated the code to include a prescription for synchrotron cooling that is based on solutions to the electron kinetic equation obtained by Kardashev (1962). If we consider an electron distribution in which fresh power-law electrons are continually injected and allowed to evolve with time in our adiabatically expanding jet, there will be a break in the spectrum due to the balance between supply and radiative cooling, found at

$$E_{br} = \frac{4}{AB^2t}, \quad (1)$$

where $A = \sigma_T / (6\pi m_e^2 c^3)$, B is the magnetic field, m_e is the electron mass. Equation 1 tells us how the break energy of the electron distribution will evolve with time, but since our model is time-independent we instead quantify the break energy analytically using characteristic timescales. We do this by setting $t = t_{dyn}$ where $t_{dyn} = \Delta z / \beta_j c$ is the dynamical time during which electrons travel through a jet segment of height Δz at a bulk-flow velocity β_j . Synchrotron cooling in balance with a continuous particle injection rate yields a broken powerlaw electron distribution given by

$$dN = \begin{cases} CE^{-p}dE, & E \leq E_{br} \\ CE^{-(p+1)}dE, & E > E_{br} \end{cases}, \quad (2)$$

where, after substituting $t = t_{dyn}$ into (1), E_{br} is given by

$$E_{br} = \frac{4\beta_j c}{AB^2\Delta z} = \frac{24\pi\beta_j m_e^2 c^4}{\sigma_T B^2 \Delta z}. \quad (3)$$

If the spectrum without cooling is given by $I_\nu \propto \nu^{-\alpha}$, then cooling produces a steepening in the spectrum from α to $\alpha + 0.5$ at the corresponding critical break frequency, $\nu_{br} = (eB/2\pi m_e c)\gamma_{br}^2$, where $\gamma_{br} = E_{br}/m_e c^2$. We can understand how the cooling break will evolve along the jet by considering its dependence on the variable quantities, $E_{br} \propto \beta_j B^{-2} \Delta z^{-1}$. Since the jet is accelerating, and the overall energy budget is inversely proportional to the Mach number (this is the dominant cooling term), we know that the particle number density and magnetic field strength

decrease with jet height. Thus it is clear that the cooling break energy will increase with jet height, suggesting that only solutions in which acceleration occurs close to the base of the jet (preliminary fits to broadband spectra from both Sgr A* and A0620 indicate an approximate range, $z_{acc} \sim 5\text{--}20 r_g$) will contain a synchrotron cooling break in the observed optically thin spectrum (at energies ranging from the IR and higher), assuming re-acceleration of the electrons in each zone.

4.2 Injection of a mixed particle distribution

The kinetics of the particles close to the black hole imply that the particle distribution will likely be mixed, i.e. some fraction of the particles will be non-thermal, with the bulk of the particles being thermal, and this is shown through previous modelling of Sgr A*'s accretion flow (e.g. Yuan, Quataert & Narayan 2003; Dibi et al. 2014). As such we modify our model in order to allow for the possibility that a mixed particle distribution is injected at the base of the jet. The thermal particles follow a Maxwell-Jüttner distribution (as in the pure thermal case) at temperature T_e , where the electrons are assumed to remain relativistic ($\gamma_{min,th} = 1$). Those electrons presumed to have been accelerated prior to injection are distributed as $dN = CE^{-p}dE$ between the limits $\gamma_{min,nth} = 2.23 kT_e/m_e c^2$ and $\gamma_{max,nth} = \Delta_{fac} (2.23 kT_e/m_e c^2)$, where Δ_{fac} is a fixed parameter, varying only on a case-by-case basis (see Section 6). The fraction of electron energy density injected into the non-thermal tail is also a model parameter, $\epsilon_{nth} = U_{nth}/U_e$, where U_{nth} is the non-thermal electron energy density, given by $U_{nth} = \int_{\gamma_{min,nth}}^{\gamma_{max,nth}} CE^{1-p}dE$. Thus ϵ_{nth} can be related to the commonly prescribed $\epsilon_e = \epsilon_{nth}/(1+k)$ which parameterises the energy given to electrons via shocks (Sari, Piran & Narayan 1998), though here we assume only that some energy is given to electrons via an unspecified acceleration process. This full distribution is then cooled both due to the jet acceleration and synchrotron emission, and we assume there is no further particle acceleration elsewhere in the jet (i.e. z_{acc} becomes an inactive parameter of `agnjet`). In each zone we adjust the limits of the power-law distribution from $\gamma = 1$ to $\gamma_{max,nth}$ in that zone in order to represent the thermalising of those non-thermal particles as they cool. The power-law distribution is then described by Equation 2. In contrast to the previous case, here we simply allow the electrons to cool along the jet without re-acceleration.

5 METHOD

We perform the spectral fits using the multiwavelength data analysis package `ISIS` (Houck & DeNicola 2000), version 1.2.6-32. `agnjet` is imported into `ISIS` and (along with other model components, such as absorption routines) forward-folded through the detector response matrices. `ISIS` also allows one to read in lower frequency data (i.e. radio through to optical) from ASCII files for simultaneous broadband fitting. Any fits shown in flux space display the “unfolded spectra,” which are independent of the assumed spectral model. The model fits to the data are performed in detector space, thus all residuals are the difference between the data and

forward-folded model counts, normalised by the uncertainty in that bin (standardised χ^2 residuals).

5.1 Fitting methodology

The individual fitting routines for Sgr A* and A0620 are as follows. The X-ray spectra obtained for Sgr A* consist of the brightest 3 of 39 total flares, as discussed in Section 4, selected based on peak count rate and total fluence (counts), ensuring we have enough photon statistics to perform our fits (see Section 5.2). The data comprise both 0th order (i.e. undispersed photons) and MEG (Medium Energy Grating) and HEG (High Energy Grating) \pm first order flares. Due to photon pileup 0th order spectra cannot be background subtracted, and are instead modelled as the superposition of a quiescent emission model (representative of the diffuse background emission around Sgr A*; Wang et al. 2013) plus `agnjet`, with a kernel accounting for pileup. The constraints of our modelling therefore tie to the thermal quiescent spectrum. It is noted that the flares show no notable emission lines (Wang et al. 2013). The MEG and HEG \pm first order spectra are background subtracted and fit with `agnjet` corrected for interstellar absorption and dust scattering. We bin all the X-ray flare spectra at $S/N = 4$, setting a minimum number of 5 channels so as to avoid spurious groupings of photon counts at adjacent energies, and we set the energy bounds at 2–9 keV. For the 0th order and 1st orders, respectively, the fit functions are `TBnew * dustscat * (agnjet + brems) + gaussian(1) + gaussian(2)` and `TBnew * dustscat * agnjet`, where `TBnew` represents interstellar absorption (Wilms, Allen & McCray 2000; Wilms et al. 2016, in prep, with cross-sections from Verner et al. 1996), and `dustscat` accounts for dust scattering (Baganoff et al. 2003). The `brems` model represents the quiescent continuum associated with Sgr A*'s accretion flow (Wang et al. 2013), with temperature $kT \sim 3.5$ keV, and the two gaussian lines represent the best fit emission lines at 2.48 keV and 6.7 keV respectively, the He-like S and Fe K α lines (these are the strongest emission lines). We adopt $M_{BH} = 4 \times 10^6 M_{\odot}$, $D = 8$ kpc, and set the jet inclination to $\theta_i = 80^\circ$ in accordance with the orbital inclination ($0.75^\circ \leq i \leq 0.85^\circ$) inferred from both broadband modelling (Markoff, Bower & Falcke 2007) and MHD simulations of Sgr A*'s accretion flow (Mościbrodzka et al. 2009; Shcherbakov, Penna & McKinney 2012; Drappeau et al. 2013).

The X-ray spectrum of A0620 is binned at a minimum of 15 counts per bin within energy bounds 0.3–8 keV in agreement with Gallo et al. (2006), such that we can perform χ^2 statistics on the multiwavelength spectra. Since the IR to UV spectrum is de-reddened prior to fitting, the fitting methodology is very simple. The X-ray spectra are fit with `TBnew * agnjet`, and the rest by `agnjet` alone. We are not concerned with line features present in the quiescent spectrum of A0620, however we do model the spectrum of the stellar companion, which dominates the near-IR - UV spectrum ($4500 \text{ K} \leq T_{star} \leq 4900 \text{ K}$ González Hernández et al. 2004; Froning et al. 2011). We allow the X-ray absorbing column N_H to vary given the uncertainty on its measured value. We adopt $M_{BH} = 6.6 M_{\odot}$, $D = 1.06$ kpc, and $\theta_i = 51^\circ$ for A0620 throughout.

For the fitting method we first make use of a fast χ^2 minimisation algorithm, and then we further explore our parameter space using an ISIS implementation (Murphy & Nowak 2014) of the Markov Chain Monte Carlo (MCMC) method of Foreman-Mackey et al. (2013). This routine makes use of the principles of an affine-invariant ensemble sampler, setting up a distribution of ‘walkers’ in the probability density landscape. These walkers explore the landscape by accepting moves based on the probability ratio of the proposed and current positions in the parameter space. In all our MCMC runs each parameter range contains > 200 walkers, all initialised uniformly within 1% of the values found from the pre-MCMC χ^2 minimisation, and allowed to evolve within flat uniform prior distributions over the area of parameter space we are exploring. Each run is allowed to evolve for at least 3000 steps in order to ensure reasonable convergence of the chain.

6 INDIVIDUAL SPECTRAL FITS

Figures 3 and 4 show separate spectral fits to the broadband spectrum of A0620 and Sgr A* respectively, covering 4 cases for each source; (a) thermal particle injection, SSC-dominated, (b) thermal particle injection, synchrotron-dominated, (c) mixed particle injection, SSC-dominated, (d) mixed particle injection, synchrotron-dominated. The corresponding maximum likelihood estimates (MLEs) and their 90% confidence regions are shown in Table 2. Here we briefly discuss the results of all 4 cases of model-fitting. Since the acceleration efficiency, f_{sc} , and the multiplication factor, Δ_{fac} , determine the cut-off in the non-thermal particle distribution (and thus the synchrotron spectrum), we choose to fix these values (f_{sc} in cases (a) and (b), Δ_{fac} in cases (c) and (d)) at their extremes. This ensures that the X-ray spectrum is fit with the non-thermal synchrotron emission in our synchrotron-dominated fits (with no cut-off present within the observing band), and the non-thermal synchrotron spectrum cuts off below X-ray energies in the SSC-dominated fits. We also note that whilst we allow the acceleration region z_{acc} to be free during fitting, due to the discretised nature of the jet axis, though z_{acc} is constrained it is not fully resolved; this is further complicated by possible correlations between z_{acc} and the other model parameters.

6.1 A0620

6.1.1 Case (a): thermal particle injection, SSC-dominated

This case corresponds to pure thermal particle injection at the jet base, with the X-ray spectrum dominated by SSC emission from the electrons in the base of the jet. The physical state portrayed is close to that found by Gallo et al. (2007) in which an older version of `agnjet` is fit to a multiwavelength spectrum of A0620 (the spectral coverage of the data in their modelling was the same, but there were fewer data points in the optical/UV bands). The jet base is relatively compact, and the magnetic energy density is sub-equipartition with respect to the electrons. Such a model class coincides with those previously found to work well for BHs in quiescence at low luminosities ($L_X \sim 10^{-9}$ – 10^{-8} ; Plotkin et al. 2015). Another distinct property we notice in

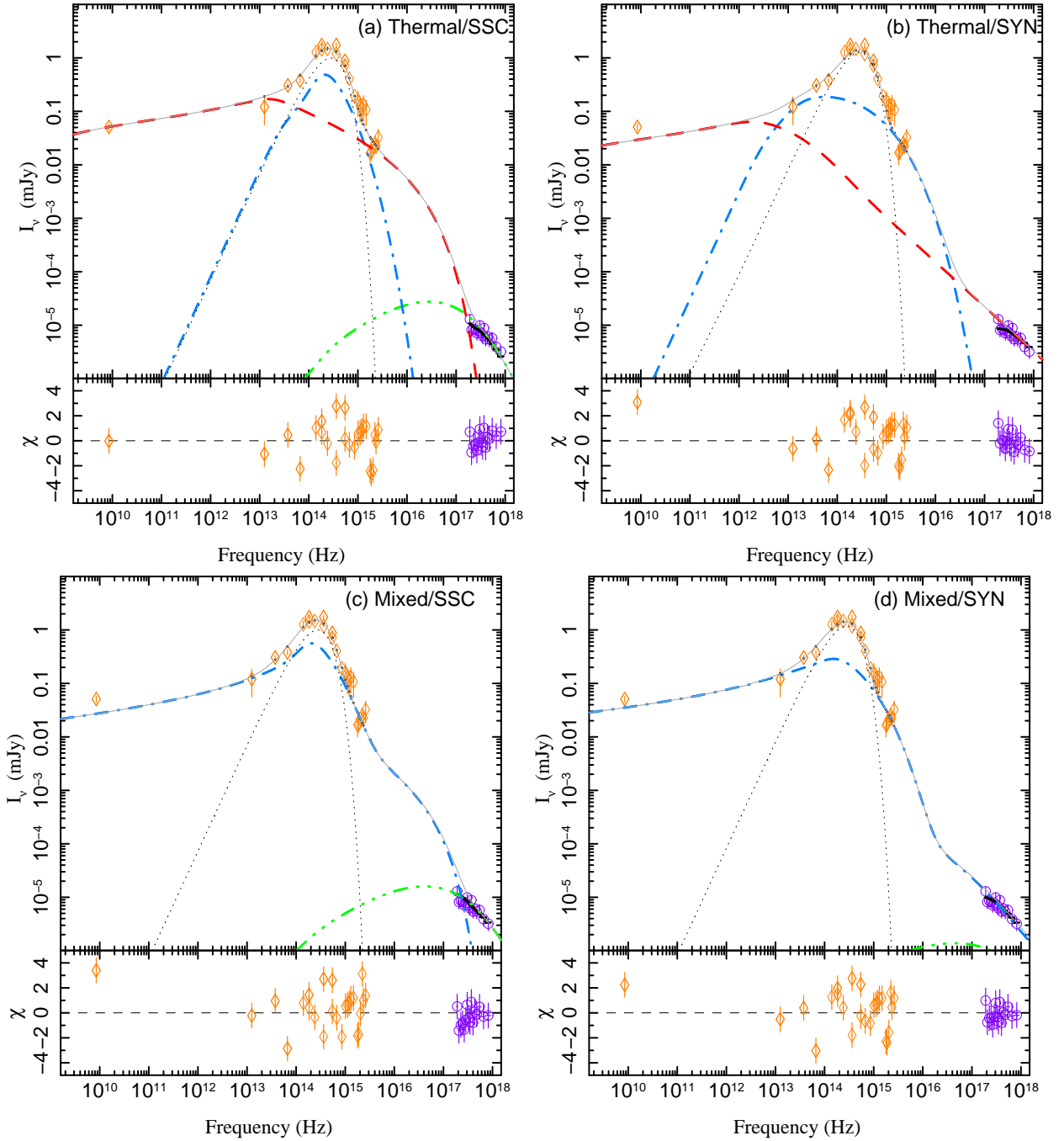


Figure 3. Spectral fits to the individual broadband spectrum of A0620. The four panels show cases (a) - (d) of our model fits to A0620. Orange diamond data points show the radio - FUV spectrum loaded into ISIS as flux density measurements. The X-ray spectrum is shown with purple circles. In each plot the absorbed model fit is indicated in thick black. In cases (a) and (b) the unabsorbed model components shown are pre-acceleration (thermal) synchrotron emission (blue dot-dashed line), post-acceleration synchrotron emission (red dashed line), SSC (green three-dot-dashed line), the blackbody spectrum of the stellar companion (black short-dashed line), and the total spectrum of *agnjet* (grey solid line). In cases (c) and (d) we do not include an explicit acceleration zone and thus there is no 'post-acceleration' spectrum. Instead the synchrotron spectrum emitted by the full thermal + non-thermal electron distribution is shown with the blue dot-dashed line, and the SSC spectrum is shown by the green three-dot-dashed line. The bottom panels of each plot show the standardised residual photon counts.

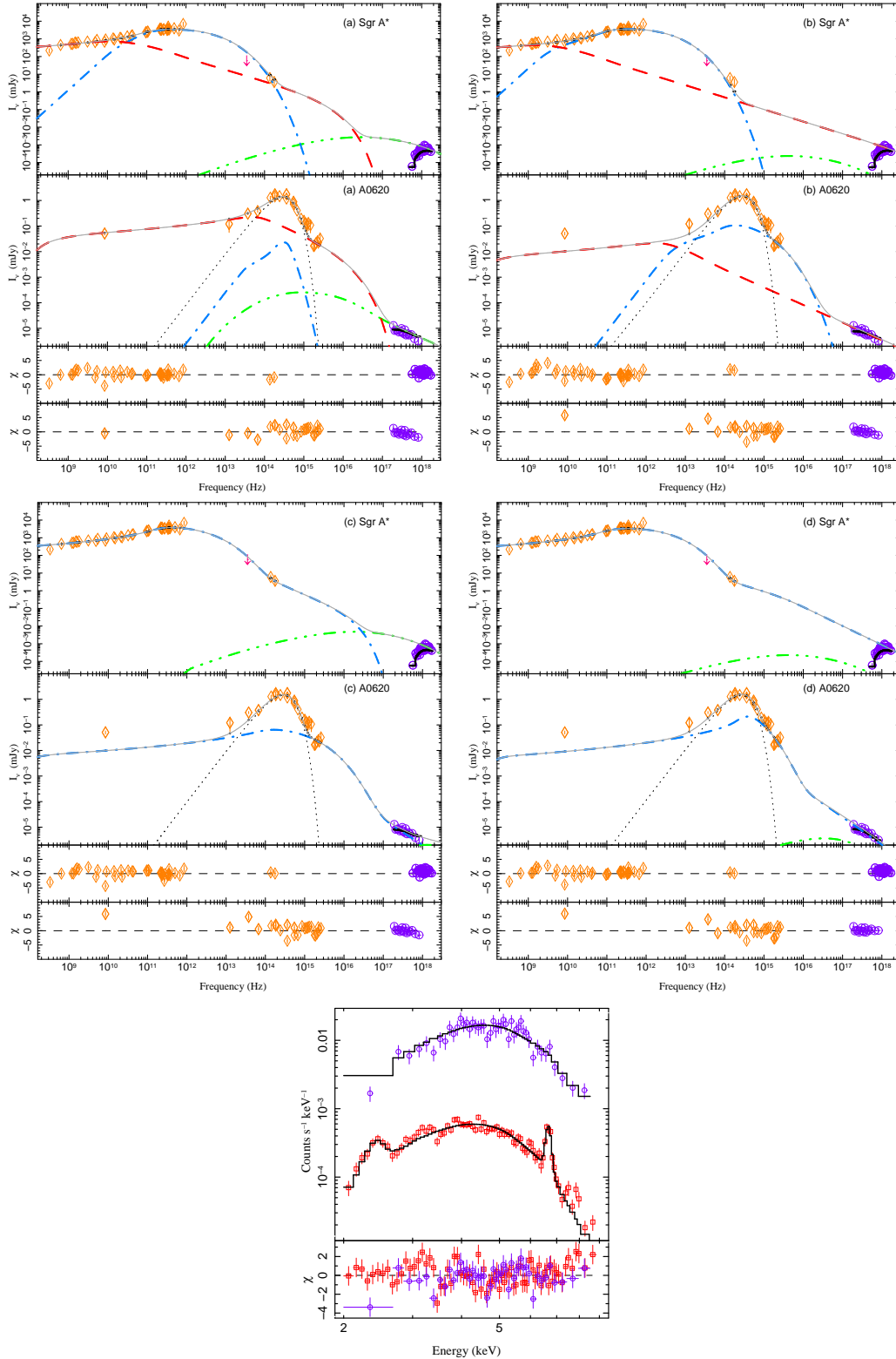


Figure 4. Spectral fits to the individual broadband spectrum of Sgr A*. The first 4 panels show cases (a) - (d) of our model fits to Sgr A*. Radio and IR observations are indicated by orange diamonds, and X-ray 1st-order grating spectra shown with purple circles. The mid-IR 3σ upper limit is shown as a downward pointing arrow. In each plot the absorbed model fit is indicated in thick black. In cases (a) and (b) (top panels) the unabsorbed model components shown are pre-acceleration (thermal) synchrotron emission (blue dot-dashed line), post-acceleration synchrotron emission (red dashed line), SSC (green three-dot-dashed line), the blackbody spectrum of the stellar companion (black short-dashed line), and the total spectrum of *agnjet* (grey solid line). In cases (c) and (d) (middle panels) we do not include an explicit acceleration zone and thus there is no ‘post-acceleration’ spectrum. Instead the synchrotron spectrum emitted by the full thermal + non-thermal electron distribution is shown with the blue dot-dashed line, and the SSC spectrum is shown by the green three-dot-dashed line. The bottom panels of each plot show the standardised residual photon counts. The bottom panel shows the 0th-order flare- (purple circles) -and-quiescent (red squares) X-ray spectra of Sgr A* and the associated model fit, representative of all

Table 2. Fitted parameters for synchrotron-and-SSC-dominated individual spectral fits to A0620 and Sgr A*. Shown are 4 model cases for fits to each source, (a) thermal particle injection, SSC-dominated, (b) thermal particle injection, synchrotron-dominated, (c) mixed particle injection, SSC-dominated, (d) mixed particle injection, synchrotron-dominated. Confidence limits are at the 90% level, a result of our MCMC exploration of the posterior distributions of the parameters. The resultant MLEs are given by the median point of each posterior distribution - this proves to be a good measure of the converged best fit of the MCMC routine. The final column shows the resultant χ^2 and the degrees of freedom (DoF). From left-to-right the following parameters are shown: N_H , the Hydrogen column density along the line-of-sight to the source, N_j , the jet power, p , the spectral index of the power-law-distributed electrons, T_e , the temperature of the electron distribution (Maxwell-Jüttner), z_{acc} , the location of acceleration in the jet (only applicable when a pure thermal particle distribution is injected at the base, cases (a) and (b)), r_0 , the radius of the jet-base nozzle, h_{ratio} the ratio of the nozzle height h_0 to the jet-base radius r_0 , k , the energy partition factor, and ϵ_{nth} , the fraction of energy density in non-thermal electrons. Jet-base electron densities ($n_{e,0}$) and magnetic field strengths (B_0) are shown for the corresponding MLEs.

Case	N_H [10^{22} cm^{-2}]	N_j [10^{-7}]	p	T_e [10^{10} K]	z_{acc} [r_g]	r_0 [r_g]	h_{ratio} [h_0/r_0]	k	ϵ_{nth} [10^{-2}]	$\frac{\chi^2}{\text{DoF}}$	$n_{e,0}$ [cm^{-3}]	B_0 [G]
A0620												
(a)	$0.2^{+0.3}_{-0.1}$	110^{+50}_{-30}	$1.7^{+0.5}_{-0.2}$	$2.5^{+0.8}_{-0.4}$	60^{+1270}_{-30}	6^{+1}_{-1}	2^{+2}_{-1}	$0.2^{+0.3}_{-0.1}$...	58/31	1.2×10^{14}	8.7×10^5
(b)	$0.15^{+0.10}_{-0.04}$	110^{+20}_{-40}	$2.7^{+0.3}_{-0.2}$	$8.5^{+0.5}_{-4.9}$	200^{+260}_{-150}	23^{+8}_{-13}	1.5^f	7^{+2}_{-6}	...	70/32	4.0×10^{11}	5.1×10^4
(c)	$0.4^{+0.4}_{-0.3}$	210^{+110}_{-60}	2^{+1}_{-1}	$3.3^{+1.3}_{-1.0}$...	10^{+3}_{-2}	$1.1^{+0.4}_{-0.4}$	$0.20^{+0.16}_{-0.09}$	< 23	77/31	7.9×10^{13}	7.3×10^4
(d)	$0.12^{+0.21}_{-0.10}$	130^{+70}_{-40}	$2.2^{+0.7}_{-0.5}$	$4.2^{+20.0}_{-0.9}$...	9^{+85}_{-1}	$0.6^{+0.8}_{-0.3}$	2^{+7}_{-1}	$0.4^{+4.8}_{-0.3}$	67/31	1.8×10^{13}	1.3×10^5
Sgr A*												
(a)	$12.5^{+0.8}_{-0.7}$	13^{+3}_{-1}	$2.0^{+0.6}_{-0.3}$	48^{+1}_{-2}	50^{+40}_{-30}	$2.2^{+0.2}_{-0.1}$	$1.2^{+0.1}_{-0.1}$	$0.003^{+0.001}_{-0.001}$...	239/181	1.3×10^7	13.7
(b)	$12.9^{+0.3}_{-1.4}$	$4.59^{+0.09}_{-0.95}$	$2.42^{+0.02}_{-0.15}$	$20.9^{+0.1}_{-0.9}$	100^{+1420}_{-20}	$3.9^{+0.4}_{-0.5}$	1.5^f	$9.5^{+0.4}_{-2.9}$...	274/182	3.1×10^5	80.3
(c)	$12.5^{+0.8}_{-0.8}$	17^{+5}_{-3}	$2.3^{+0.5}_{-0.6}$	$40.8^{+0.2}_{-0.6}$...	$2.02^{+0.05}_{-0.02}$	$0.85^{+0.05}_{-0.03}$	$0.002^{+0.001}_{-0.001}$	3^{+4}_{-2}	257/181	2.4×10^7	14.4
(d)	$13.2^{+0.9}_{-0.7}$	$4.6^{+0.1}_{-0.2}$	$2.00^{+0.1}_{-0.1}$	$18.95^{+0.05}_{-0.18}$...	$4.1^{+0.40}_{-0.2}$	1.5^f	$9.7^{+0.3}_{-0.8}$	$0.8^{+0.9}_{-0.4}$	327/182	3.0×10^5	76.1

Notes. ^f Frozen parameter

this model fit when compared to cases (b), (c) and (d), is that the radio and X-ray spectra are fit simultaneously with ease.

6.1.2 Case (b): thermal particle injection, synchrotron-dominated

The synchrotron-dominated fit shows broadly different physical specifications, with higher electron temperatures than those seen in case (a), a slightly less compact jet base, and again a roughly equipartition magnetic field with respect to the electrons. No cooling break exists within the limits of the non-thermal particle distribution. This is because in all synchrotron-dominated fits in which particle acceleration occurs only at z_{acc} , the fits evolve to solutions in which the acceleration region is too high for efficient cooling to occur ($B_{z_{acc}} \sim 0.14B_0$, where B_0 is the jet-base magnetic field strength).

6.1.3 Case (c): mixed particle injection, SSC-dominated

Here again the X-ray spectrum is SSC-dominated, except the injected distribution carries a fraction ϵ_{nth} of non-thermal energy. This fraction is poorly constrained here since it influences the synchrotron emission more than the SSC emission, but it must nonetheless be a small fraction (< 23%). As in case (a) the electrons are constrained to fairly low temperature and the jet base is compact and well constrained. The magnetic field is sub-equipartition, and the jet power is high and statistically distinguishable from the ranges found for cases (a) and (b), albeit not well constrained. It is not obvious that this is a physical difference, it is more likely that the method by which we divide energy between thermal and non-thermal particles in each case causes a systematic change to the injected power.

6.1.4 Case (d): mixed particle injection, synchrotron-dominated

If again we assume a small fraction of the particles present at the jet base are non-thermal, we can explain the X-ray spectrum with synchrotron emission from those non-thermal particles, provided non-thermal particles carry just a small fraction of the total particle energy ($< 5.2\%$, see Table 2). The particles must however have been accelerated quite efficiently, with their cut-off extending to $10^4 \gamma_{min}$, and a cooling break between UV/X-ray energies at $\sim 10^{17}$ Hz. Again we find the jet power must be systematically higher when we inject this mixed distribution of particles in comparison to the pure thermal case, which again may simply be due to how we divide the energy between the particles. There is an increase in the upper limit on the electron temperature when compared with the SSC-dominated fit (inspection of the probability distribution reveals a bi-modal behaviour), and the system also tends towards a slightly super-equipartition magnetic field with respect to the electrons.

6.2 Sgr A*

In all fits to Sgr A* the mid-IR upper limit ($I_{8.6\mu m} < 58 \text{ mJy}$, Haubojs et al. 2012) sets a rough flat prior on the upper limits of T_e and k . In a mildly sub-equipartition regime ($k \sim 0.1\text{--}0.5$) we find an approximate upper limit on the electron temperature of $T_e \sim 3 \times 10^{11}$ K (and poor fits to the X-ray flare spectrum). Thus, in this regime, the brightest X-ray flares detected around Sgr A* cannot be explained by SSC emission as long as the plasma remains in equilibrium (see however Dibi et al. 2014). To achieve higher temperatures and thus satisfactorily model the X-ray flares, we require a much more sub-equipartition flow ($k \sim 10^{-3}$). Figure 4 (panels (a) and (c)) shows SSC-dominated fits in which the jet energy partition has fallen to values of $k \sim 10^{-3}$, and in this case, we find that an electron temperature of $T_e > 4 \times 10^{11}$ K provides a good fit to the full spectrum without violating the mid-IR upper limits.

6.2.1 Case (a): thermal particle injection, SSC-dominated

Here we require an electron temperature $T_e > 4.6 \times 10^{11}$ K, with a highly sub-equipartition magnetic energy density in order to model the X-ray flare spectrum of Sgr A*. The size of the acceleration region is roughly consistent with the flare timescales, though too large when considering the brightest flares; Neilsen et al. 2013; Barri re et al. 2014). The NIR fluxes weakly constrain the electron power law index (producing non-thermal synchrotron emission, consistent with those found by Bremer et al. (2011): $\alpha \sim 0.7 \pm 0.4$, thus $p \sim 2.4 \pm 0.8$). We do not see any strong correlation between T_e and k in this local fit landscape, implying that once we go to very sub-equipartition conditions, the electron temperature must always be high.

6.2.2 Case (b): thermal particle injection, synchrotron-dominated

In this case we are able to model the X-ray flare spectrum with uncooled non-thermal synchrotron emission, in which

the magnetic field is in rough equipartition with the electrons. Particle acceleration occurs at a region (z_{acc}) that is roughly consistent with the range of flare timescales, though again not consistent with the timescales of brightest flares (Barri re et al. 2014); solutions like this in which particle acceleration occurs further out in the jet are thus unlikely.

6.2.3 Case (c): mixed particle injection, SSC-dominated

Assuming we have a fraction ϵ_{nth} of non-thermal energy in non-thermal electrons in our jet also allows us to successfully model the Sgr A* X-ray flare spectrum in the SSC-dominated case (given a highly sub-equipartition magnetic energy density), though it should be noted that the thermal synchrotron spectrum reaches the mid-IR upper limit. The NIR spectrum is fit partially with the thermal synchrotron turnover, but is dominated by synchrotron emission from the non-thermal tail of electrons. We notice that the fit also tends towards a more compact jet base and a high jet power, which is an attempt to boost the SSC flux to match the X-ray spectrum (as inverse Comptonisation depends strongly on the electron density), though as mentioned in Section 6.1, the systematic increase in power when injecting a mixed particle distribution may be a natural consequence of how we divide energy between the particles.

6.2.4 Case (d): mixed particle injection, synchrotron-dominated

A scenario in which particle acceleration occurs within a few r_g of the black hole favours the flare timescales of Sgr A*, and such solutions are preferred in other more detailed modelling of the accretion flow close to the black hole (Yuan, Quataert & Narayan 2003; Dibi et al. 2014). Our synchrotron-dominated fit within this scenario explains both the IR and X-ray flare spectra, with slightly super-equipartition conditions at the jet base. A small fraction of the electron energy is in non-thermal electrons, producing a hard non-thermal synchrotron tail that fits the IR emission, and the X-ray spectrum is then well modelled by synchrotron emission from the cooled electrons, with a break at $\sim 10^{16}$ Hz. It should however be noted that the thermal synchrotron flux sits at the mid-IR upper limit.

7 JOINT FITTING

As seen in the individual spectral fits (Section 6), the ranges of the potential scaling parameters (which we shall now discuss) are comparable for all models, which leads well into exploring joint fits with these parameters tied. The technique used when fitting `agnjet` jointly to A0620 and Sgr A* follows the same logic as with individual fits. Each data set is loaded into ISIS, and the model definitions are split as described in Section 6, except we now require almost the same model for both Sgr A* and A0620.

Following the theoretical prescription of Markoff et al. (2003) and Heinz & Sunyaev (2003), we assume that scale invariance manifests itself in geometric quantities such as r_0 , h_0 , and z_{acc} , and so we choose to tie these together for both sources. We tie a further 2 parameters by presuming that the division of energy and the acceleration mechanisms are

roughly coincident at similar accretion rate in the sources that fit on the FP (k and p); both these parameters are key to understanding whether there are fundamental differences in the energy partition of sources at very quiescent levels, and also whether spectral indices may differ (Russell et al. 2013; Plotkin et al. 2015). By tying these 5 parameters together, we both explore the extent to which black holes can be treated as scale-invariant, as well as potentially breaking some of the model degeneracies. Parameters that we expect to depend explicitly on cooling and the physical values of the electron density and magnetic field (e.g. T_e) would not be expected to scale with black hole mass, and are thus left to vary accordingly. We effectively equate the f_{sc} parameter for both sources by freezing its value at its extremes in the SSC/synchrotron-dominated cases as described in Section 6. We refer the reader to Table 3 for all parameter values mentioned in the following presentation of the results. We now discuss the 4 cases of joint fits just as in Section 6, that cannot be ruled out relative to one another in terms of their goodness-of-fit, but we discuss which areas of parameter space are less favourable given what we know about the behaviour of Sgr A* and A0620.

7.1 Case (a): thermal particle injection, SSC-dominated

Here we achieve good fits to the data given a very sub-equipartition magnetic field, but the electron temperature still needs to be high in order to produce the required X-ray flux via pure SSC emission. The fit to A0620 sees a statistically significant decrease in the jet-base radius compared with individual spectral fits, whilst this value is consistent with single fits of this case to Sgr A* (see section 6). This property applies independently of the type of model we are fitting (though SSC-dominated fits, i.e. cases (a) and (c), give slightly more compact jet bases). The electron temperature of A0620's inner accretion flow also decreases, and the particle acceleration zone (z_{acc}) drops compared with individual fits. A significant change is seen for the jet power of A0620, which has to increase to account for the drop in the energy partition parameter (and thus a reduced magnetic field strength), an effect displayed clearly in Figure 6, showing the two-dimensional confidence contours of parameters in which we see correlations.

7.2 Case (b): thermal particle injection, synchrotron-dominated

Here we see that the result of tying z_{acc} during synchrotron-dominated fits is to push its value higher to allow the A0620 X-ray spectrum to be modelled sufficiently, and this also results in tighter constraints on its value. Solutions in which particle acceleration occurs so distant from the black hole are unlikely to be the source of bright X-ray flares given the timescale constraints on Sgr A*'s X-ray variability (Nielsen et al. 2013; Barri re et al. 2014); we expect the flare emission to be originating from within $\sim 5 r_g$ of the black hole during the brightest flares. One notices a few correlations in the 2D contours shown in Figure 6, including a weak but persistent positive correlation between N_j and k for Sgr A* and A0620 during these synchrotron-dominated

states. This implies that by providing energy to the magnetic field in Sgr A*, the drop in electron density is enough to force an increase in the injected power; fits to Sgr A*, even in the synchrotron-dominated case, are very sensitive to electron density.

7.3 Case (c): mixed particle injection, SSC-dominated

Figure 5 shows, similar to case (a), that the mid-IR constraints on the jet-base electron temperature result in a significantly reduced partition factor. This is consistent with the case (c) single fit to Sgr A*, but significantly lower than single fits to A0620. The electron temperature of Sgr A* is high, even with such a sub-equipartition flow, and the mid-IR limits are almost surpassed. The electron temperature of Sgr A* remains consistent with single fits, but we see a statistically significant increase in the electron temperature of A0620, again reflecting the evolution to a highly sub-equipartition magnetic field (reflected in the jet-base magnetic field values shown in Table 3). We also note that whilst we see a correlation between r_0 and T_e in single fits to A0620, this correlation is not present in our joint fits, a possible indication that the joint fitting approach indeed reduces some of the physical degeneracy. The value of ϵ_{nth} is statistically indistinguishable between Sgr A* and A0620, though we note that for A0620 its value is constrained to lower fractions than those in the fit to Sgr A*. There is a k - r_0 weak anti-correlation introduced by performing this joint fit, which may reflect the relative importance of the energy partition over the electron temperature (this is evident also from the weak constraints we are able to place on T_e). We also note that, as shown in Figure 5, the X-ray spectrum of A0620 is dominated by the synchrotron emission from the non-thermal tail injected at the base of the jet, indicating that in this case the mass-scaling changes the phenomenology of this class of fit to A0620.

7.4 Case (d): mixed particle injection, synchrotron-dominated

Here we see a fast-cooling dominated synchrotron spectrum, produced by a population of accelerated electrons close to the black hole, consistent with the observed timescales of the flares (Barri re et al. 2014). Russell et al. (2013) indicate that BHBs that decline into quiescence seem to exhibit a cooling-break evolution down to UV energies. We find cooling breaks for both Sgr A* and A0620 at $\sim 10^{16}$ Hz and $\sim 10^{17}$ Hz respectively. Whilst the values of p and ϵ_{nth} remain consistent with single fit values for both Sgr A* and A0620, other parameters show statistically significant changes. Sgr A*'s jet power is decreased, T_e and r_0 drop in the A0620 fit, and Sgr A*'s inner flow goes to slightly lower energy partition, decreasing the jet-base magnetic field. We note that just as in case (c), the T_e - r_0 correlation in A0620 fits is removed when fitting jointly, however Figure 6 shows that a correlation is introduced between T_e and N_j for both Sgr A* and A0620.

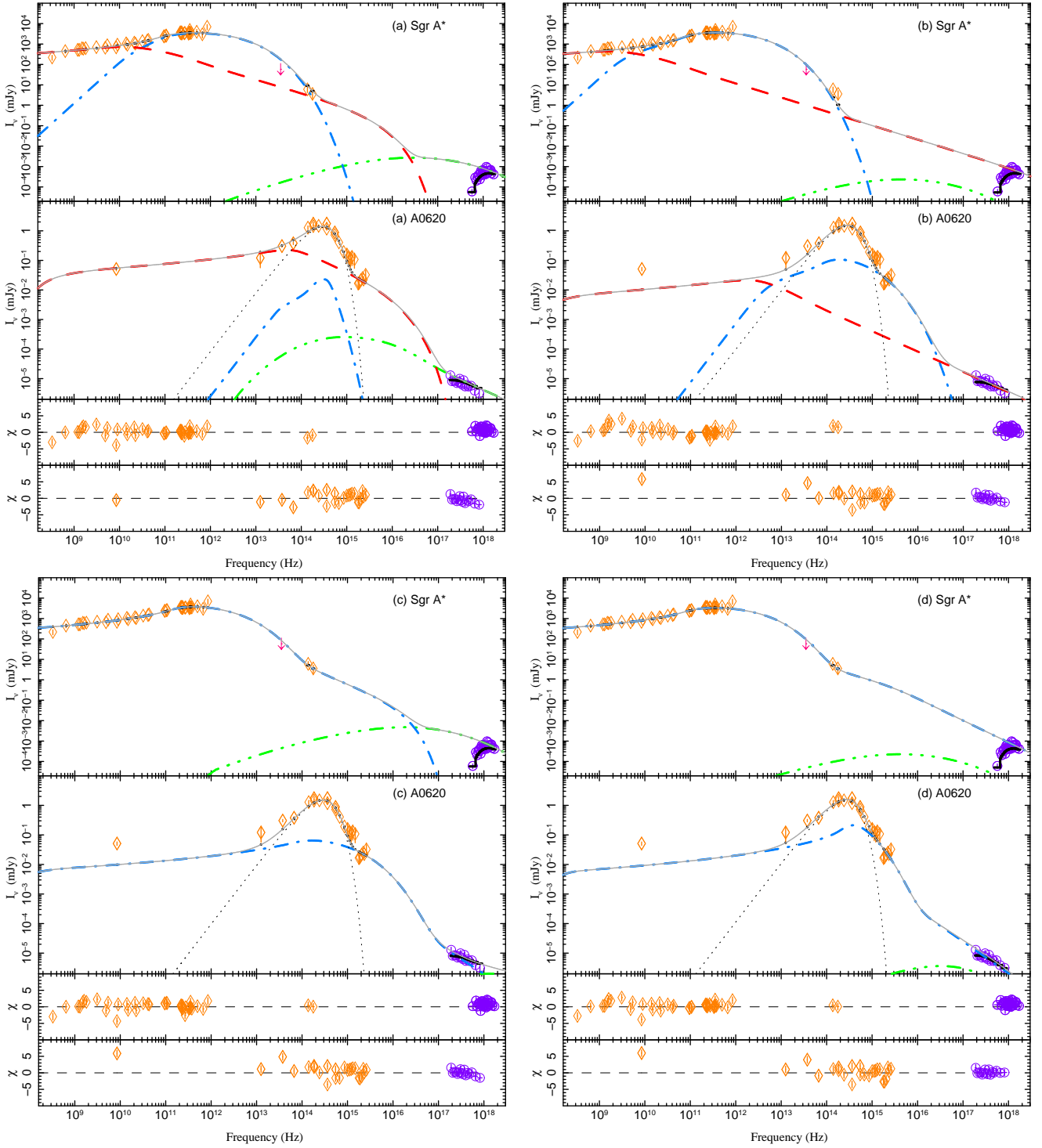


Figure 5. Joint spectral fits to both the Sgr A* and A0620-00 spectrum. The top left panel shows the case (a) model fit, top right the case (b) model fit, bottom left the case (c) model fit, and bottom right the case (d) model fit, where the Sgr A* and A0620 plots are indicated. In all A0620 plots the Orange diamonds show the radio - FUV spectrum loaded into ISIS as flux density measurements, and the 1st-order grating X-ray spectrum is shown with purple circles. In all Sgr A* plots the orange diamonds show radio - IR data loaded into ISIS as flux density measurements, with the X-ray spectrum in purple points. The model fit is indicated in black. In cases (a) and (b) the unabsorbed model components shown are pre-acceleration (thermal) synchrotron emission (blue dot-dashed line), post-acceleration synchrotron emission (red dashed line), SSC (green three-dot-dashed line), the blackbody spectrum of the stellar companion (black short-dashed line), and the total spectrum of *agnjet* (grey solid line). In cases (c) and (d) we do not include an explicit acceleration zone and thus there is no 'post-acceleration' spectrum. Instead the synchrotron spectrum emitted by the full thermal + non-thermal electron distribution is shown with the blue dot-dashed line, and the SSC spectrum is shown by the green three-dot-dashed line. The bottom panels of each plot show the standardised residual photon counts. In cases (a) and (b) parameters r_0 , h_{ratio} (though this is fixed in case (b)), z_{acc} , p and k are tied, and in cases (c) and (d) we tie the same parameters except for z_{acc} , which does not function in these cases.

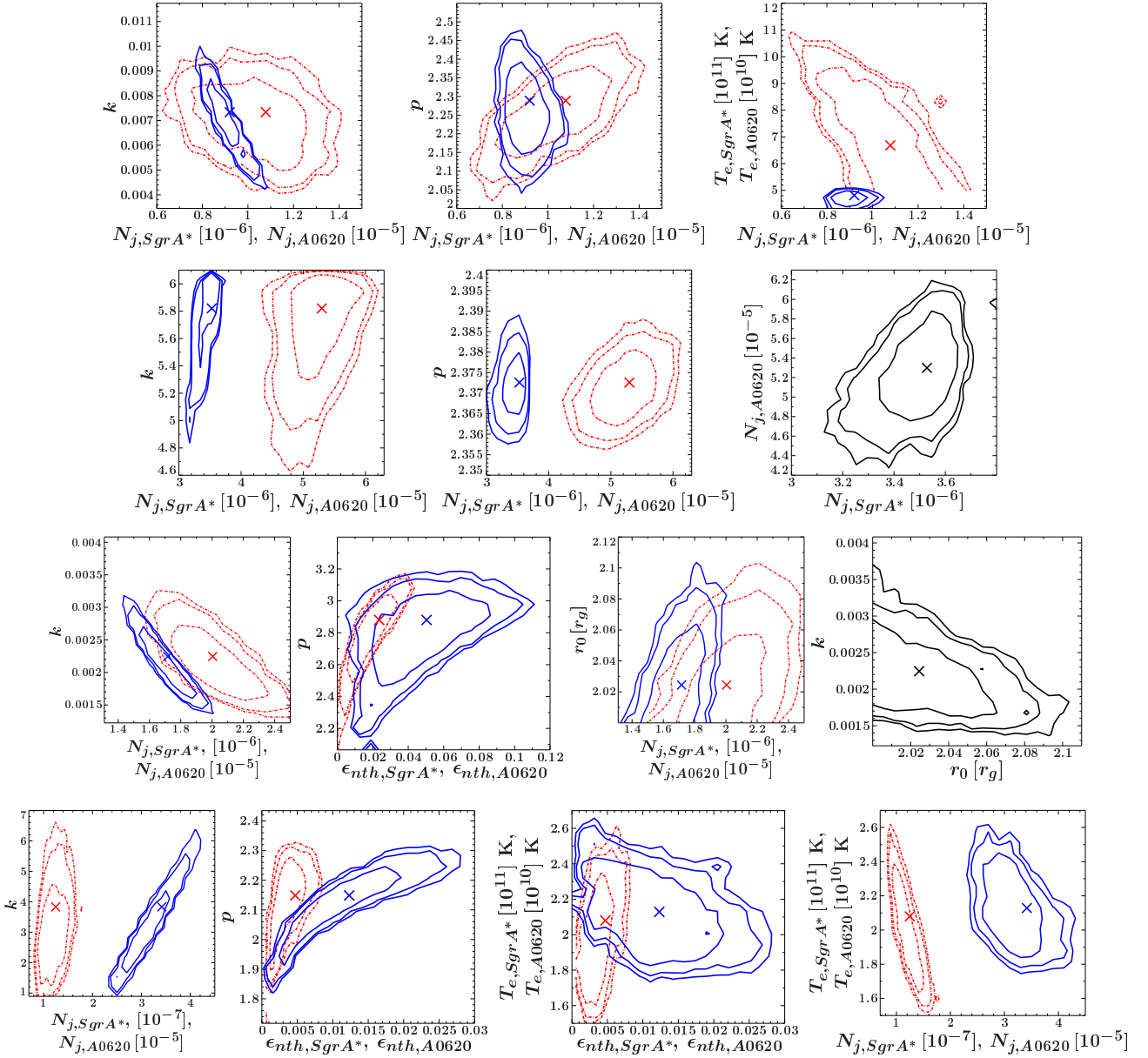


Figure 6. Two-dimensional contours of parameters of interest in joint fits to Sgr A* and A0620, covering all 4 cases, (a) - (d), shown consecutively from the top row of panels (case (a)) to the bottom row of panels (case (d)). Blue solid lines show contours at 0.68/0.90/0.95 confidence for Sgr A* fitted parameters, and red dotted lines show the equivalent for A0620 parameters. Black solid lines show contours either for joint-fitted parameters or comparisons between a parameter applying to each source individually. The crosses indicate the MLEs.

8 DISCUSSION AND CONCLUSION

We have shown that mass-scaling in weakly accreting black holes (the FP) can be exploited to break degeneracies in spectral modelling. This has been explored for higher luminosity, hard-state-like sources by [Markoff et al. \(2015\)](#); here we extend this study for the first time to the most quiescent sources. We find that the majority of key parameters can be tied in the modelling of Sgr A* and A0620, namely the jet-base radius r_0 , the distance from the black hole along the jet axis at which particle acceleration occurs z_{acc} , the height of the jet nozzle h_0/r_0 , the partition of energy between the magnetic field and electrons k , and the

spectral index of the accelerated electron distribution p . This new approach reduces the strength of some parameter correlations (i.e. degeneracy) and better constrains those tied parameters, leading to more informative distinctions between different model classes.

Our results imply that if the X-ray spectrum of Sgr A* during the brightest flares is dominated by SSC emission from a purely thermal population of electrons, its jet-base magnetic field must be significantly sub-equipartition, and the electron temperatures push to high values, giving rise to mid-IR fluxes close to the upper limit obtained by [Haubois et al. \(2012\)](#). If indeed A0620

Table 3. Fitted parameters for Synchrotron-and-SSC-dominated joint spectral fits to A0620 and Sgr A*. Shown are 4 model cases for fits, (a) thermal particle injection, SSC-dominated, (b) thermal particle injection, synchrotron-dominated, (c) mixed particle injection, SSC-dominated, (d) mixed particle injection, synchrotron-dominated. Confidence limits are at the 90% level, a result of our MCMC exploration of the posterior distributions of the parameters. The resultant MLEs are given by the median point of each posterior distribution - this proves to be a good measure of the converged best-fit of the MCMC routine. The final column shows the resultant χ^2 and the degrees of freedom (DoF). From left-to-right the following parameters are shown: N_H , the Hydrogen column density along the line-of-sight to the source, N_j , the jet power, p , the spectral index of the power-law-distributed electrons, T_e , the temperature of the electron distribution (Maxwell-Jüttner), z_{acc} , the location of acceleration in the jet (only applicable when a pure thermal particle distribution is injected at the base, cases (a) and (b)), r_0 , the radius of the jet nozzle, h_{ratio} the ratio of the nozzle height h_0 to the jet-base radius r_0 , k , the energy partition factor, and ϵ_{nth} , the fraction of energy density in non-thermal electrons. The parameters r_0 , h_{ratio} , z_{acc} , p , and k are tied together where applicable (in cases (c) and (d) there is no acceleration zone in the jet, and thus z_{acc} is null.) Jet-base electron densities ($n_{e,0}$) and magnetic field strengths (B_0) are also shown for the corresponding MLEs.

Source	N_H [10^{22} cm^{-2}]	N_j [10^{-7}]	p	T_e [10^{10} K]	z_{acc} [r_g]	r_0 [r_g]	h_{ratio} [h_0/r_0]	k	ϵ_{nth} [10^{-2}]	$\frac{\chi^2}{\text{DoF}}$	$n_{e,0}$ [cm^{-3}]	B_0 [G]
(a)												
Sgr A*	$11.8_{-0.7}^{+0.6}$	$9.2_{-0.8}^{+1.2}$...	48_{-2}^{+2}	8.3×10^6	17.4
A0620	$0.15_{-0.05}^{+0.19}$	1100_{-300}^{+200}	...	$0.7_{-0.2}^{+0.3}$	3.8×10^{16}	1.5×10^5
Joint	$2.3_{-0.2}^{+0.1}$...	20_{-5}^{+9}	$2.27_{-0.19}^{+0.08}$	$1.22_{-0.07}^{+0.12}$	$0.007_{-0.002}^{+0.002}$...	329/219
(b)												
Sgr A*	$12.2_{-0.7}^{+0.7}$	$3.5_{-0.2}^{+0.1}$...	$20.9_{-0.5}^{+0.1}$	3.5×10^5	66.9
A0620	$0.14_{-0.03}^{+0.09}$	53_{-6}^{+6}	...	$4.7_{-0.7}^{+1.4}$	1.4×10^{13}	2.0×10^5
Joint	$2.37_{-0.01}^{+0.01}$...	180_{-20}^{+10}	$4.0_{-0.2}^{+0.3}$	1.5^f	$5.8_{-0.8}^{+0.3}$...	406/220
(c)												
Sgr A*	$12.3_{-0.7}^{+0.7}$	17_{-2}^{+2}	...	$41.7_{-0.8}^{+0.3}$	5_{-3}^{+4}	...	2.3×10^7	14.8
A0620	$0.14_{-0.03}^{+0.09}$	200_{-20}^{+40}	...	17_{-5}^{+2}	< 3	...	3.8×10^{14}	3.9×10^4
Joint	$2.9_{-0.4}^{+0.2}$	$2.02_{-0.02}^{+0.06}$	$0.85_{-0.03}^{+0.05}$	$0.002_{-0.001}^{+0.001}$...	390/218
(d)												
Sgr A*	$13.4_{-0.8}^{+0.9}$	$3.4_{-0.8}^{+0.7}$...	21_{-3}^{+3}	$1.2_{-0.9}^{+1.2}$...	5.4×10^5	67.7
A0620	$0.20_{-0.09}^{+0.11}$	120_{-30}^{+30}	...	$2.1_{-0.4}^{+0.4}$	$0.5_{-0.3}^{+0.3}$...	1.2×10^{14}	3.2×10^5
Joint	$2.1_{-0.2}^{+0.1}$	$3.7_{-0.3}^{+0.4}$	$1.08_{-0.07}^{+0.12}$	4_{-2}^{+2}	...	381/218

Notes. f Frozen parameter

and Sgr A* can be related via their energy partition, then we would expect sources accreting at $l_X \sim 10^{-9}$ – 10^{-8} to be highly sub-equipartition.

An alternative physical scenario in which the X-ray spectra of A0620 and Sgr A* are dominated by synchrotron emission from an injected non-thermal distribution of electrons is consistent with what we know about the variability of Sgr A* (as opposed to the solutions we find in which particle acceleration occurs in regions $> 5 r_g$ from the black hole Barrière et al. 2014), and can also explain the broadband spectra of both sources. In this scenario, a small fraction (\sim a few %, statistically consistent for both Sgr A* and A0620) of the injected electron energy

density is in non-thermal electrons, and these electrons experience a cooling break at $\sim 10^{16}$ Hz and $\sim 10^{17}$ Hz for Sgr A* and A0620 respectively. These results are consistent with previous modelling of Sgr A* that indicates a cooling break in the synchrotron spectrum between IR and X-ray energies (Dibi et al. 2012, 2014). We therefore find that the suggestion of Markoff (2010) and Plotkin et al. (2015) that quiescent BHBs enter a regime of inefficient particle acceleration is an inherently degenerate one. The effect of inefficient acceleration (and therefore SSC-dominated X-ray states) can be subsumed by efficient particle cooling within the peak synchrotron emission zones. This interpretation is consistent with the

findings of [Russell et al. \(2013\)](#) that as BHBs evolve to quiescence their cooling breaks evolve to lower frequencies such that the break may be observed in the UV band. We also note that recent single-zone modelling of the inner accretion flow of Sgr A*, with the goal of reproducing the observed IR/X-ray flare distributions, shows that particle acceleration as well as density and magnetic field changes are key to producing the flares ([Dibi et al. 2016](#)).

Both these scenarios are consistent with a matter-dominated disc-jet system, in which the jet magnetisation is low ([Blandford & Payne 1982](#)), as opposed to a Poynting-flux dominated jet in which we should expect high magnetisations ([Blandford & Znajek 1977](#)). As discussed in section 4, we are unable to properly describe a highly magnetised jet with our model, since we explicitly assume $U_B \leq nm_p c^2$. However, we note that a scenario in which the jet has a Poynting-dominated spine surrounded by a matter-dominated outer sheath may still be consistent with the conditions we find ([Hawley & Krolik 2006](#); [Mościbrodzka, Falcke & Noble 2016](#)).

Achieving efficient particle acceleration, whether via internal shocks or magnetic reconnection, is an ongoing area of study, with some recent progress coming from PIC simulations of both such mechanisms (e.g. [Sironi & Spitkovsky 2011, 2014](#); [Sironi, Spitkovsky & Arons 2013](#); [Sironi, Petropoulou & Giannos 2015](#)). In the shock-acceleration scenario (assuming quasi-perpendicular shocks), it proves difficult to accelerate electrons to high energies unless the pre-shock conditions are at low magnetisation. Conversely in the magnetic reconnection scenario, electrons may be accelerated to high energies if the inner regions are highly magnetised. We propose that at the most quiescent levels ($l_X \sim 10^{-9}$ – 10^{-8}) accreting black holes struggle to achieve the structures necessary for efficient particle acceleration (as represented by the acceleration regions at $z > z_{acc}$), but that there are still likely a small fraction of non-thermal radiating particles at the jet base (in the fast-cooling regime) of the black hole produced via another acceleration mechanism ([Yuan, Quataert & Narayan 2003](#)). We also propose that such sub-equipartition conditions at the jet base favour brighter SSC emission in the X-rays, which reinforces the findings of [Plotkin et al. \(2015\)](#) that a switch to quiescence in BHBs is associated with a compact jet base (a few gravitational radii) and sub-equipartition magnetic fields with respect to the electrons. These sub-equipartition magnetic fields may coincide with the production of weakly magnetised outflows as opposed to highly collimated jets.

We can understand more about what each mechanism (synchrotron or SSC) predicts in terms of the emission timescales of Sgr A*'s daily flares, in particular the connection between X-ray and IR emission, by considering the timescales for particle acceleration in weakly relativistic outflows. An electron with a Lorentz factor γ gyrating in a magnetic field B , will have a peak synchrotron frequency of

$$\nu = \frac{q\gamma^2 B}{2\pi m_e c} \Rightarrow \gamma \approx 3 \times 10^4 \left(\frac{B}{100 \text{ G}} \right)^{-1/2} \left(\frac{h\nu}{1 \text{ keV}} \right)^{1/2}. \quad (4)$$

From Equation 4, we can see that electrons with energies ~ 15 GeV will be capable of radiating X-rays in a 100 G strength magnetic field.

The time it takes for an electron to be accelerated to an energy capable of radiating at a given frequency ν in diffusive shock acceleration (DSA) is (e.g., [Caprioli & Spitkovsky 2014](#))

$$t_{acc} = \frac{6D(\epsilon)}{v_s^2}, \quad (5)$$

where the v_s is the velocity of the upstream flow in the downstream reference frame relative to the shock. If we assume that the particle acceleration happens in the Bohm diffusion limit, the diffusion coefficient is (e.g., [Jokipii 1987](#); [Amato 2015](#))

$$D_B(\epsilon) = \frac{cr_L}{3}; \quad r_L = \frac{\gamma mc^2}{qB}. \quad (6)$$

Combining Equations (4), (5), and (6) yields the following acceleration time:

$$\begin{aligned} t_{acc} &= \frac{2c^2 r_L}{v_s^2 c} \\ &\approx 1.3 \times 10^{-4} \left(\frac{B}{100 \text{ G}} \right)^{-3/2} \left(\frac{h\nu}{1 \text{ keV}} \right)^{1/2} \left(\frac{v_s}{0.5c} \right)^{-2} \text{ s}. \end{aligned} \quad (7)$$

We assumed shock acceleration to derive Equation (7), but a derivation assuming magnetic reconnection would yield a similar result for the minimum acceleration time, (e.g. [Kumar & Crumley 2015](#)):

$$\begin{aligned} t_{acc} &= \frac{1}{\epsilon_0} \frac{r_L}{c} \\ &\sim 2 \times 10^{-4} \left(\frac{B}{100 \text{ G}} \right)^{-3/2} \left(\frac{h\nu}{1 \text{ keV}} \right)^{1/2} \left(\frac{\epsilon_0}{0.1} \right)^{-1} \text{ s}. \end{aligned} \quad (8)$$

$\epsilon_0 = E/B_0 \leq 1$ is the reconnection rate, and simulations find an $\epsilon_0 \sim 0.1$ (e.g. [Kagan, Milosavljević & Spitkovsky 2013](#)). The fastest particles can be accelerated roughly the same whether the particles are accelerated via shocks or magnetic reconnection in a mildly relativistic outflow.

During a flare, t_{acc} is the smallest time we should expect the X-rays to lag the IR photons (assuming the IR photons are produced by electrons at the initial stage of acceleration). The lag time is so small we should expect the infrared and X-rays to be simultaneous. For example the X-ray lags on minute timescales (with respect to IR emission) reported by [Yusef-Zadeh et al. \(2012\)](#)—who argue an inverse Compton origin for the X-ray flares—are unlikely to be explained by delayed particle acceleration and subsequent synchrotron emission in both bands. If further studies of the coupling between the IR/X-ray variability of Sgr A* indicated that the IR lags the X-ray, synchrotron emission would not be able to explain the observed time lag. This calculation does not, however, take into account synchrotron cooling of the electrons during the acceleration process, which is one of our predicted scenarios. Also we consider here only the time to accelerate particles, not the time delays we may expect for shocks or magnetic reconnection events to develop in a relativistic outflow, which is an interesting further point to explore in the context of Sgr A*'s IR/X-ray variability. For example, as discussed in section 1, studies of Sgr A*'s X-ray variability

have allowed inferences regarding the particle acceleration process, with many finding magnetic reconnection to be a viable process, likely in a fast-cooling regime (Neilsen et al. 2013; Li et al. 2015; Dibi et al. 2016)—we note that this supports our synchrotron-dominated model scenario.

Our new joint-fitting technique strongly favours a scenario in which the most sub-Eddington accreting black holes (quiescence down to $l_X \sim 10^{-9} - 10^{-8}$) have very compact jet bases, on the order of a few gravitational radii. This holds regardless of whether the emission is dominated by non-thermal synchrotron from a population of accelerated electrons (accelerated within a few r_g of the black hole), or a high-density sub-equipartition flow which produces dominant SSC emission (or potentially a mixture of these two processes). We find that the particle acceleration component in the outer jet recedes, leaving evidence for another kind of weak acceleration in the inner accretion flow (Yuan, Quataert & Narayan 2003), or an inverse Compton-dominated jet base. We echo the statements made by Plotkin et al. (2015) that further well-sampled SEDs of quiescent BHs are required to draw more precise conclusions regarding the accretion/jet dynamics and local conditions, in particular breaking the degeneracy between synchrotron or SSC domination in such weakly accreting systems, and what is driving the change from one regime to another. In addition to this, the efforts of the Event Horizon Telescope (EHT) (Doeleman et al. 2008) to probe the inner regions of Sgr A*’s accretion flow will shed light on local plasma conditions, and may reveal more about the plausibility of these model scenarios. A parallel strategy is to improve our modelling, and in the near future we will implement self-consistent, relativistic MHD flow solutions to reduce the free parameters in our jet modelling, in particular the geometrical quantities and their relationship to the internal properties (e.g. Polko, Meier & Markoff 2010, 2013, 2014). This will be presented in an upcoming paper (Ceccobello et al., in prep).

In the future we hope to build further upon our results here based upon more recent broadband observations (X-ray/radio/optical-IR) of A0620 (e.g. MacDonald, Bailyn & Buxton 2015) that may give more insight into the outflow structure of A0620. Such insights would come primarily from the radio spectrum of A0620, since in our modelling we are limited by the lack of radio coverage (with only the 8.5 GHz flux).

ACKNOWLEDGEMENTS

This research has made use of ISIS functions provided by ECAP/Remeis observatory and MIT (<http://www.sternwarte.uni-erlangen.de/ISIS/>).

RC is thankful for support from NOVA (Dutch Research School for Astronomy). SM and RC are grateful to the University of Texas in Austin for its support through a Tinsley Centennial Visiting Professorship. RC thanks Rik van Lieshout for useful discussions on the use of Markov Chain Monte Carlo in parameter exploration.

REFERENCES

Amato E., 2015, arXiv:1503.02399

- An T., Goss W. M., Zhao J.-H., Hong X. Y., Roy S., Rao A. P., Shen Z.-Q., 2005, ApJ, 634, L49
- Baganoff et al., 2001, Nature, 413, 45
- Baganoff et al., 2003, ApJ, 591, 891
- Barrière N. M. et al., 2014, ApJ, 746, 46
- Belloni T., 2010, in Belloni T., ed., Lect. Notes Phys. Vol. 794, The Jet Paradigm - From Microquasars to Quasars
- Blandford R. D., Begelman M. C., 1999, MNRAS, 303, L1
- Blandford R. D., Begelman M. C., 2004, MNRAS, 349, 68
- Blandford R. D., Payne D. G., 1982, MNRAS, 199, 883
- Blandford R. D., Znajek R. L., 1977, MNRAS, 179, 433
- Bower G. C., Wright M. C. L., Falcke H., Backer D. C., 2003, ApJ, 588, 331
- Bower G. C. et al., 2015, ApJ, 802, 69
- Brinkerink C. D., et al., 2015, A&A, 576, A41
- Bremer M. et al., 2011, A&A, 532, A26
- Cantrell A. G. et al., 2008, ApJ, 673, L159
- Cantrell A. G. et al., 2010, ApJ, 710, 1127
- Caprioli D., Spitkovsky A., 2014, ApJ, 794, 47
- Casella P. et al., 2010, MNRAS, 404, L21
- Corbel S., Fender R. P., Tzioumis A. K., Nowak M., McIntyre V., Durouchoux P., Sood R., 2000, A&A, 359, 251
- Corbel S., Nowak M., Fender R. P., Tzioumis A. K., Markoff S., 2003, A&A, 400, 1007
- Corbel S., Tomsick J. A., Kaaret P., 2006, ApJ, 636, 971
- Corbel S., Körding E., Kaaret P., 2008, MNRAS, 389, 1697
- Corbel S., Coriat M., Brocksopp C., Tzioumis A. K., Fender R. P., Tomsick J. A., Buxton M. M., Bailyn C. D., 2013, MNRAS, 428, 2500
- Dibi S., Drappeau S., Fragile P. C., Markoff S., Dexter J., 2012, MNRAS, 426, 1928
- Dibi S., Markoff S., Belmont R., Mazlac J., Barrière N. M., Tomsick J. A., 2014, MNRAS, 441, 1005
- Dibi S., Markoff S., Belmont R., Malzac J., Neilsen J., Witzel G., 2016, MNRAS, 461, 552
- Dodds-Eden et al., 2011, ApJ, 728, 37
- Doeleman S. S. et al., 2008, Nature, 455, L78
- Drappeau S., Dibi S., Dexter J., Markoff S., Fragile P. C., 2013, MNRAS, 431, 287
- Eckart A. et al. 2006, A&A, 450, 535
- Elvis M., Page C. G., Pounds K. A., Ricketts M. J., Turner M. J. L., 1975, Nature, 257, 656
- Falcke H., 1996, ApJ, 464, L67
- Falcke H., Biermann P., 1995, A&A, 293, 665
- Falcke H., Markoff S., 2000, A&A, 362, 113
- Falcke H., Goss W. M., Matsuo H., Teuben P., Zhao J. H., Zylka R., 1998, ApJ, 499, 731
- Falcke H., Körding E., Markoff S., 2004, A&A, 414, 895
- Falcke H., Markoff S., Bower G. C., 2009, A&A, 496, 77
- Fender R. P., 2001, MNRAS, 322, 31
- Foreman-Mackey D., Hogg D. W., Lang D., Goodman J., 2013, PASP, 125, 306
- Froning C. S. et al., 2011, ApJ, 743, 26
- Gallo E., Fender R. P., Pooley G. G., 2003, MNRAS, 344, 60
- Gallo E., Fender R. P., Miller-Jones J. C. A., Merloni A., Jonker P. G., Heinz S., Maccarone T. J., van der Klis M., 2006, MNRAS, 370, 1351
- Gallo E., Migliari S., Markoff S., Tomsick J. A., Bailyn C. D., Berta S., Fender R., Miller-Jones J. C. A., 2007, ApJ, 670, 600
- Gallo E. et al., 2014, MNRAS, 445, 290
- Gandhi P. et al. 2010, MNRAS, 390, L29
- Garcia M. R., McClintock J. E., Narayan R., Callanan P., Barret D., Murray S. S., 2001, ApJ, 553, L47
- Genzel R., Eisenhauer F., Gillessen S., 2010, Rev. Mod. Phys., 82, 4
- Genzel et al., 2003, Nature, 425, 934
- Ghez A. M. et al., 2004, ApJ, 601, L159

- Ghez A. M. et al., 2008, *ApJ*, 689, 1044
 Gierliński M., Done C., 2003, *MNRAS*, 342, 1083
 Gillessen S., Eisenhauer F., Trippe S., Alexander T., Genzel R., Martins F., Ott T., 2009, *ApJ*, 692, 1075
 González Hernández A. I., Rebolo R., Isrealian G., Casares J., Maeder A., Meynet G., 2004, *ApJ*, 609, 988
 Hawley J. F., Krolik J. H., 2006, *ApJ*, 641, 103
 Heinz S., Sunyaev R. A., 2003, *MNRAS*, 343, L59
 Hornstein et al., 2007, *ApJ*, 667, 900
 Houck J. C., DeNicola L. A., 2000, in Manset N., Veillet C., Crabtree D., eds, *ASP conf. Ser. Vol. 216, Astronomical Data Analysis Software and Systems IX*. Astron. Soc. Pac., San Francisco, p.159
 Haubois X. et al., 2012, *A&A*, 540, A41
 Jkipii J. R., 1987, *ApJ*, 313, 842
 Kagan D., Milosavljević M., Spitkovsky A., 2013, *ApJ*, 774, 41
 Kalamkar M. et al., 2016, *MNRAS*, 460, 3284
 Kardashev N. S., 1962, *SvA*, 6, 317
 Kong A. K. H., McClintock J. E., Garcia M. R., Murray S. S., Barret D., 2002, *ApJ*, 570, 277
 Körding E., Falcke H., Corbel S., 2006, *A&A*, 456, 439
 Körding E., Jester S., Fender R., 2006, *MNRAS*, 372, 1366
 Kumar P., Crumley P., 2015, *MNRAS*, 453, 1820
 Lasota J.-P., 2001, *NewAR*, 45, 449
 Li Y.-P. et al., 2015, *ApJ*, 810, 19
 Lu R.-S., Krichbaum T. P., Eckart A., König S., Kunnerath D., Witzel G., Witzel A., Zensus J. A., 2011, *A&A*, 525, A76
 MacDonald, Bailyn, Buxton, presentation at AAS meeting 225 at Seattle WA, U.S., 04-08 January 2015, https://files.aas.org/aas225/AAS225A_bstracts.pdf, (accessed June 08, 2016)
 Maitra D., Markoff S., Brocksopp C., Noble M., Nowak M., Wilms J., 2009, *MNRAS*, 398, 1638
 Markoff S., 2005, *ApJ*, 618, L103
 Markoff S., 2010, *PNAS*, 107, 7196
 Markoff S., Bower G. C., Falcke H., 2007, *MNRAS*, 379, 1519
 Markoff S., Falcke H., Yuan F., Biermann P. L., 2001, *A&A*, 379, L13
 Markoff S., Nowak M., Corbel S., Fender R. P., Falcke H., 2003, *A&A*, 397, 645
 Markoff S., Nowak M., Wilms J., 2005, *ApJ*, 635, 1203
 Markoff S. et al., 2008, *ApJ*, 681, 905
 Markoff S. et al. 2015, in prep.
 Marrone D. P., Moran J. M., Zhao J.-H., Rao R., 2006, *ApJ*, 640, 308
 McClintock J. E., Remillard R. A., 1986, *ApJ*, 308, 110
 McClintock J. E., Remillard R. A., 2000, *ApJ*, 531, 956
 McHardy I. M., Körding E. G., Knigge C., Uttley P., Fender R. P., 2006, *Nature*, 444, 730
 Melia F., Falcke H., 2001, *ARA&A*, 39, 309
 Merloni A., Heinz S., Di Matteo T., 2003, *MNRAS*, 345, 1057
 Miller-Jones J. C. A., McCormick D. G., Fender R. P., Spencer R. E., Muxlow T. W. B., Pooley G. G., 2005, *MNRAS*, 363, 867
 Miller-Jones J. C. A., Jonker P. G., Maccarone T. J., Nelemans G., Calvelo D. E., 2011, *ApJ*, 739, L18
 Mościbrodzka M., Gammie C. F., Dolence J. C., Shiokawa H., Leung P. K., 2009, *ApJ*, 706, 497
 Mościbrodzka M., Falcke H., Noble S., 2016, preprint, arXiv:1610.08652
 Muno M. P., Mauerhan J., 2006, *ApJ*, 648, L135
 Murphy K. D., Nowak M. A., 2014, *ApJ*, 797, 12
 Narayan R. D., Yi I., 1994, *ApJ*, 428, 2291
 Narayan R. D., Yi I., Mahedevan R., 1995, *Nature*, 374, 623
 Narayan R. D., McClintock J. E., Yi I., 1996, 457, 821
 Neilsen J. et al., 2013, *ApJ*, 774, 42
 Neilsen J. et al., 2015, *ApJ*, 799, 199
 Nord M. E., Lazio T. J. W., Kassim N. E., Goss W. M., Duric N., 2004, *ApJ*, 601, L51
 Nowak M. A., 1995, *PASP*, 107, 1027
 Nowak M. A. et al., 2011, *ApJ*, 728, 13
 Nowak M. A. et al., 2012, *ApJ*, 759, 95
 Plotkin R. M., Markoff S., Kelly B. C., Körding E., Anderson S. F., 2012, *MNRAS*, 419, 267
 Plotkin R. M., Gallo E., Jonker P. G., 2013, *ApJ*, 773, 59
 Plotkin R. M., Gallo E., Markoff S., Homan J., Jonker P. G., Miller-Jones J. C. A., Russell D. M., Drappeau S., 2015, *MNRAS*, 446, 4098
 Polko P., Meier D. L., Markoff S., 2010, *ApJ*, 723, 1343
 Polko P., Meier D. L., Markoff S., 2013, *MNRAS*, 428, 587
 Polko P., Meier D. L., Markoff S., 2014, *MNRAS*, 438, 959
 Predehl P., Schmitt J.H.M.M., 1995, *A&A*, 293, 889
 Prieto M. A., Fernández-Ontiveros J. A., Markoff S., Espada D., González z-Martín O., 2016, *MNRAS*, 457, 3801
 Quataert E., 2002, *ApJ*, 575, 855
 Reid M. J., 1993, *ARA&A*, 31, 345
 Reid M. J. et al., 2009, *ApJ*, 700, 137
 Remillard R. A., McClintock J. E., 2006, *ARA&A*, 44, 49
 Roy S., Rao P., 2004, *MNRAS*, 349, L25
 Russell D. M., Fender R. P., 2008, *MNRAS*, 387, 713
 Russell D. M. et al., 2013, *MNRAS*, 429, 815
 Sari R., Piran T., Narayan R., 1998, *ApJ*, 497, L17
 Serabyn E., Carlstrom J., Lay O., Lis D. C., Hunter T. R., Lacy J. H., Hills R. E., 1997, *ApJ*, 490, L77
 Shabhz T., Fender R. P., Watson C. A., O'Brien K., 2008, *ApJ*, 672, 510
 Shakura N. I., Sunyaev R. A., 1973, *A&A*, 24, 337
 Shcherbakov R. V., Penna R. F., McKinney J. C., 2012, *ApJ*, 755, 133
 Sironi L., Spitkovsky A., 2011, *ApJ*, 726, 75
 Sironi L., Spitkovsky A., 2014, *ApJ*, 783, L21
 Sironi L., Spitkovsky A., Arons J., 2013, *ApJ*, 771, 54
 Sironi L., Petropoulou M., Giannos D., 2015, *MNRAS*, 450, 183
 Stirling A. M., Spencer R. E., de la Force C. J., Garrett M. A., Fender R. P., Ogle R. N., 2001, *MNRAS*, 327, 1273
 Tomsick J. A. et al., 2003, *ApJ*, 593, L133
 Tomsick J. A., Kalemci E., Kaaret P., 2004, *ApJ*, 601, 439
 Trap G. et al., 2011, *A&A*, 528, 140
 Uttley P., McHardy I. M., 2005, *MNRAS*, 363, 586
 van der Klis M., 1995, in Lewin W. H. G., van Paradijs J., van den Heuvel E. P. J., eds, *X-ray Binaries*. p. 252
 Verner D. A., Ferland G. J., Korista K. T., Yakovlev D. G., 1996, *ApJ*, 465, 487
 Wang et al., 2013, *Science*, 341, 981
 Wilms J., Allen A., McCray R., 2000, *ApJ*, 542, 914
 Wilms J., Juett A. M., Schulz N. S., Nowak M. A., 2016, in preparation
 Witzel G. et al., 2012, *ApJ*, 203, 18
 Yuan F., Markoff S., Falcke H., 2002, *A&A*, 383, 854
 Yuan F., Quataert E., Narayan R., 2003, *ApJ*, 598, 301
 Yuan F., Cui W., Narayan R., 2005, *ApJ*, 620, 905
 Yuan F., Narayan R., 2014, *ARA&A*, 52, 529
 Yusef-Zadeh F. et al., 2012, *ApJ*, 141, 1
 Zdziarski A., 2016, *A&A*, 586, A18
 Zhao J. H., Bower G. C., Goss W. M., 2001, *ApJ*, 547, L29
 Zylka R., Mezger P. G., Ward-Thompson D., Duschl W. J., Lesch H., 1995, *A&A*, 297, 83

APPENDIX A: BROADBAND SPECTRA OF Sgr A* AND A0620

Table A1. A0620 radio-to-FUV spectrum

ν (Hz)	I_ν (mJy)	Instrument
8.50×10^9	0.051 ± 0.007	VLA ^a
1.25×10^{13}	0.121 ± 0.065	<i>Spitzer</i> ^a
3.75×10^{13}	0.305 ± 0.031	<i>Spitzer</i> ^a
6.66×10^{13}	0.380 ± 0.038	<i>Spitzer</i> ^a
1.40×10^{14}	1.275 ± 0.188	ANDICAM (CTIO) ^b
1.84×10^{14}	1.738 ± 0.240	<i>SMARTS</i> ^a
1.84×10^{14}	1.443 ± 0.120	ANDICAM (CTIO) ^b
2.40×10^{14}	1.471 ± 0.136	ANDICAM (CTIO) ^b
3.62×10^{14}	1.744 ± 0.161	<i>SMARTS</i> ^a
3.62×10^{14}	1.184 ± 0.065	ANDICAM (CTIO) ^b
5.46×10^{14}	0.880 ± 0.065	<i>SMARTS</i> ^a
5.46×10^{14}	0.718 ± 0.059	ANDICAM (CTIO) ^b
6.71×10^{14}	0.406 ± 0.037	ANDICAM (CTIO) ^b
8.56×10^{14}	0.192 ± 0.003	UVOT (<i>Swift</i>) ^b
1.01×10^{15}	0.159 ± 0.080	STIS (<i>HST</i>) ^b
1.11×10^{15}	0.127 ± 0.063	STIS (<i>HST</i>) ^b
1.20×10^{15}	0.114 ± 0.057	STIS (<i>HST</i>) ^b
1.30×10^{15}	0.132 ± 0.066	STIS (<i>HST</i>) ^b
1.47×10^{15}	0.108 ± 0.054	STIS (<i>HST</i>) ^b
1.78×10^{15}	0.017 ± 0.007	COS (<i>HST</i>) ^b
1.87×10^{15}	0.017 ± 0.005	COS (<i>HST</i>) ^b
2.04×10^{15}	0.022 ± 0.002	COS (<i>HST</i>) ^b
2.22×10^{15}	0.025 ± 0.002	COS (<i>HST</i>) ^b
2.34×10^{15}	0.022 ± 0.006	COS (<i>HST</i>) ^b
2.60×10^{15}	0.033 ± 0.014	COS (<i>HST</i>) ^b

Notes. ^a Data taken from Gallo et al. (2006, 2007).

^b Data taken from Froning et al. (2011)

Table A2. Sgr A*radio-to-submm spectrum

ν (GHz)	I_ν (mJy)	Instrument
0.33	220 ± 60	VLA ^c
0.64	450 ± 100	GMRT ^a
1.2	520 ± 90	VLA ^a
1.3	520 ± 60	VLA ^a
1.5	620 ± 60	VLA ^a
1.6	592 ± 28	VLA ^d
1.8	630 ± 50	VLA ^a
3.1	702 ± 32	VLA ^d
4.86	660 ± 40	VLA ^a
5.4	870 ± 118	VLA ^d
8.46	690 ± 30	VLA ^a
9	932 ± 129	VLA ^d
14	1075 ± 135	VLA ^d
14.9	920 ± 60	VLA ^a
21.1	1164 ± 52	VLA ^d
22.4	1060 ± 60	VLA ^a
32	1382 ± 87	VLA ^d
40.9	1485 ± 73	VLA ^d
43	1600 ± 200	VLA ^c
95	2376 ± 187	ALMA ^e
97	2403 ± 186	ALMA ^e
105	2555 ± 197	ALMA ^e
107	2597 ± 231	ALMA ^e
216.8	3677 ± 762	SMA ^d
218	3667 ± 650	ALMA ^d
220	3661 ± 652	ALMA ^d
223.9	3391 ± 489	SMA ^d
230	3300 ± 300	JCMT ^a
231.9	3676 ± 664	ALMA ^d
233.8	3704 ± 680	ALMA ^d
238.2	3310 ± 424	SMA ^d
266.8	3369 ± 96	SMA ^d
274	3526 ± 697	SMA ^d
331.1	3205 ± 1074	SMA ^d
338.3	3436 ± 863	SMA ^d
341.6	3602 ± 866	ALMA ^d
343.6	3609 ± 870	ALMA ^d
351.7	3595 ± 884	ALMA ^d
352.6	4890 ± 721	SMA ^d
353.6	3553 ± 860	ALMA ^d
375	3500 ± 500	JCMT ^a
500	4000 ± 1200	JCMT ^a
666	3000 ± 1000	JCMT ^a
850	7000 ± 2000	CSO-JCMT ^b

Notes. Data taken from Zylka et al. (1995)^a, Serabyn et al. (1997)^b, An et al. (2005)^c, Bower et al. (2015)^d, and Brinkerink et al. (2015)^e, shown from low-to-high frequency.